

Fast, gusty winds blowing from the core of the pre-planetary nebula M 2-56

C. Sánchez Contreras¹, C. Cortijo-Ferrero², L.F. Miranda^{2,3}, A. Castro-Carrizo⁴, and V. Bujarrabal⁵

ABSTRACT

We report optical long-slit spectra and direct imaging (ground-based and with *HST*) of the pre-planetary nebula (pPN) M2-56 obtained at different epochs. The optical nebula is composed by shock-excited material distributed in two pairs of nested lobes with different sizes and surface brightness. The compact, bright inner lobes (ILs) have an angular size of $\sim 1''.5 \times 1''$ each and display closed, bow-shaped ends. The extended, faint outer lobes (OLs), which enclose the inner ones, have an angular size of $\sim 13'' \times 10''$. Within the ILs and the OLs the velocity increases with the distance to the center, however, the ILs show expansion velocities larger than the OLs. Consistent with the large speeds reached by the ILs (of up to $\sim 350 \text{ km s}^{-1}$ at the tips), we have measured the expansive proper motions of the knots ($\Delta\theta_t \sim 0''.03 \text{ yr}^{-1}$) by comparing *HST* images taken in 1998 and 2002. Moreover, we have discovered remarkable changes with time in the continuum and line emission spectrum of M 2-56. In 1998, we detected a burst of H α emission from the nebula nucleus that is interpreted as an indication of a dense, fast ($\sim 350\text{-}500 \text{ km s}^{-1}$) bipolar wind from the nebula's core (referred to as "F1-wind"). Such a wind has been recently ejected (after 1989) probably as

¹Departamento de Astrofísica, Centro de Astrobiología, CSIC-INTA, Ctra de Torrejon a Ajalvir, km 4, 28850 Torrejon de Ardoz, Madrid, Spain; csanchez@cab.inta-csic.es

²Instituto de Astrofísica de Andalucía-CSIC, C/ Glorieta de la Astronomía s/n E-18008 Granada, Spain; clara@iaa.es, lfm@iaa.es

³Departamento de Física Aplicada, Facultade de Ciencias, Universidade de Vigo E-36310 Vigo, Spain

⁴Institut de Radioastronomie Millimétrique, 300 Rue de la Piscine, F-38406 Saint Martin d'Hères, France; ccarrizo@iram.fr

⁵Observatorio Astronómico Nacional, Apartado 112, Alcalá de Henares, E-28803 Madrid, Spain; v.bujarrabal@oan.es

short-duration mass-loss event. Our data also reveal an optically thick compact cocoon (or shell-like structure) and a H II region around the central star that result from further post-AGB mass-loss after the F1-wind. Recent brightening of the scattered stellar continuum as well as an increase of scattered H α emission along the lobes is reported, both results pointing to a decrease of the optical depth of the circumstellar material enshrouding the star. The data presented here unveil the complex post-AGB mass-loss history of this object, whose rapid evolution is driven by multiple episodes of mass outflow, not regularly spaced in time, leading to: (i) acceleration of the molecular envelope that surrounds the optical nebula (kinematical age $t_k \sim 1400$ yr – Castro-Carrizo et al., 2002), (ii) the OLs ($t_k \sim 350$ -400 yr), (iii) the ILs ($t_k \sim 40$ yr), (iv) the F1-wind ($t_k < 10$ yr), and (v) the nuclear cocoon and H II region ($t_k \lesssim 2$ yr?). The successive multiple post-AGB winds in M 2-56 are characterized by ejection speeds increasing with time. In contrast, the mass-loss rate and linear momentum show a time decreasing trend.

Subject headings: stars: AGB and post-AGB, stars: mass loss, circumstellar matter, ISM: jets and outflows, planetary nebulae: general

1. Introduction

Planetary nebulae (PNe) evolve from Asymptotic Giant Branch (AGB) stars after a brief ($\approx 10^3$ yr), intermediate stage known as the pre-Planetary Nebula (pPN) or post-AGB phase. During the AGB to PN transition dramatic transformations occur: the spherical, slowly expanding ($V_{\text{exp}} \sim 15$ km/s) circumstellar envelope (CSE) expelled during the AGB becomes a nebula with, usually, clear departures from sphericity and fast (~ 100 km/s) outflows directed along one or more axes. The varied PN and pPN morphologies include not only axisymmetric (elliptical and bipolar) shells but also multipolar (multiaxial) structures, multiple co-axial shells, highly collimated jet-like ejections sometimes arranged in a point-symmetric structure, etc (e.g. Sahai et al. 1998, 2007; Ueta et al. 2007; Siódmiak et al. 2008). Most of the observed PN and pPN morphologies are difficult to explain without invoking the action of precessing, perhaps episodic, collimated outflows (e.g. Miranda et al. 1999; Guerrero et al. 2001; Miranda et al. 2006). In fact, collimated outflows are considered as the main shaping agent of PNe through their interaction with the spherical AGB CSE (Sahai & Trauger 1998).

The existence of very young, high velocity bipolar jets in some PPNe and evolved AGB stars is evidenced, for example, by water maser observations (e.g. Imai et al. 2002; Imai 2007; Suárez et al. 2009, and references therein). In some pPNs/PNs, fast, post-AGB winds are also revealed by P-Cygni profiles in the H α (and other recombination lines) emission close to the central star (Sánchez Contreras & Sahai 2001; Sánchez Contreras et al. 2008). In spite of the growing evidence of jet-like ejections in PPNs, their origin, nature (episodic or continuous?), typical mass-loss rates, life-times, etc, are still very poorly known. Detailed studies of PPNs are crucial to obtain information about the properties and dynamics of post-AGB winds and their evolution. Optical spectroscopic observations of pPNs and PNs are particularly useful for probing the post-AGB winds and their interaction with the CSE formed in the previous AGB phase.

This work focuses on the pPN M 2-56 (= IRAS 23541+7031= PK 118+08), which so far remains relatively poorly characterized, especially in the visible. A ground-based optical image obtained by Goodrich (1991, hereafter G91) showed a $\sim 10'' \times 2''$ bipolar nebula with its long axis oriented in the East-West direction (P.A.= 90°). The limited quality of this image (PSF $\sim 1''.6$ and low S/N) impeded a correct identification of the different nebular components in M 2-56 revealed by data presented in this work. High-angular resolution optical images obtained with the *HST* have been used as complementary data by Siódmiak et al. (2008) and Castro-Carrizo et al. (2002) although a detailed study based on these images has not been done so far. The *HST* images show that the bright nebulosity referred to as the “West lobe” by G91 is resolved into two compact lobes ($\sim 1''.5 \times 1''$) emerging from the center. The emission line optical spectrum of M 2-56, with strong forbidden lines of low-excitation ions, indicates major excitation by shocks (Goodrich 1991; Trammell et al. 1993; Riera et al. 2006). The lack of substantial polarization in the observed line spectrum implies that the latter is locally produced in the shock-excited lobes of M 2-56 and that there is not a significant contribution by line emission from the central regions reflected by the nebular dust (“scattered spectrum”, Trammell et al. 1993). (In this work we show that this situation has recently changed). The optical spectrum of M 2-56 also shows a weak red continuum that is the light from a B-type central star attenuated and/or partially reflected by circumstellar dust (Cohen & Kuhi 1977).

A detailed study of the dynamics and morphology of the molecular envelope of M 2-56 with high-angular resolution was carried out by Castro-Carrizo et al. (2002). Interferometric CO mapping shows an incomplete $\sim 30'' \times 15''$ hourglass-like envelope surrounding the optical lobes and similarly oriented to the latter in the plane of the sky. The inclination of the symmetry axis of the CO envelope with respect to the plane of the sky is estimated to be $i=17^\circ \pm 2^\circ$, with the East side of the nebula tilted towards us. The densest molecular material lies at the center, where the intersection of the two bipolar lobes shapes an equatorial

ring/torus expanding at $7\text{-}8\text{ km s}^{-1}$. Two compact CO clumps are found at the tips of each lobe expanding axially with velocities of $\sim 100\text{-}200\text{ km s}^{-1}$. The total mass and linear momentum of the molecular envelope of M2-56 is $M_{\text{mol}}=0.05 M_{\odot}$ and $P_{\text{mol}}=2 M_{\odot}\text{ km s}^{-1}$, adopting a distance to the source of $d=2.1\text{ kpc}$ and a standard value of the CO-to- H_2 relative abundance of $X(\text{CO})=2\times 10^{-4}$. The morphology and dynamics of the bipolar nebula is interpreted as the result of the interaction between fast, collimated post-AGB ejections and the slow CSE formed during the AGB phase. The Hubble-type expansion of the molecular outflow suggests that such an interaction took place approximately 1400 yr ago in a relatively short time, $\lesssim 300\text{ yr}$.

In this paper we will adopt a distance to M2-56 of $d=2.1\text{ kpc}$ based on the detailed discussion and final estimate by Castro-Carrizo et al. (2002). As estimated by these authors, for such a distance, the luminosity of M2-56 obtained by integrating its spectral energy distribution (SED) from the optical to the mm-wavelength range is $\sim 5500 L_{\odot}$.

In this work, we report multi-epoch optical long-slit spectra and images of M2-56 that have allowed us to describe the structure, kinematics, physical conditions, and mass-loss history of this object with unprecedented detail. Our results are discussed in terms of the formation and evolution of M2-56, which is currently in rapid transition from the AGB to the PN stage and presents clear signs of on-going, variable wind activity at the nucleus. A summary of our findings is given in Section 8.

2. Observations and data reduction

2.1. Optical Imaging

2.1.1. Ground-based images

We have obtained broad- and narrow-band images of M2-56 using the Wide Field Camera (WFC) at the prime focus of the 2.5m INT of the Roque de los Muchachos Observatory (La Palma, Spain). Observations were performed on service time mode on June 13th, 2009. The WFC consists of 4 thinned EEV $2\text{k}\times 4\text{k}$ CCDs. The CCDs have a pixel size of $13.5\ \mu\text{m}$ corresponding to $0''.33$ per pixel. Our target was observed with the chip CCD4, which has a field of view of $\sim 12'\times 23'$. Two filters were used: $\text{H}\alpha$ ($\lambda_c=6568\text{\AA}$, $\text{FWHM}=95\text{\AA}$) and Harris R ($\lambda_c=6380\text{\AA}$, $\text{FWHM}=1520\text{\AA}$). The integration times were about 530 and 2400 s for the R and $\text{H}\alpha$ images, respectively. The compact, nuclear regions of M2-56 are saturated in the $\text{H}\alpha$ image. The weather was good during the observations and the seeing was about $1''.3\text{-}1''.5$.

Images have been debiased and flat field corrected following the standard procedure

using IRAF¹. Individual frames have been registered and combined for each filter to produce final images shown in Fig. 1.

2.1.2. *HST* images

We have used two ($H\alpha$ and continuum) high angular resolution images of M2-56 from the *HST* archive. The $H\alpha$ image was obtained with the WFPC2 PC camera using the narrow band filter F656N ($\lambda_c=6564\text{\AA}$, FWHM=21.5 \AA) on 1998-09-04 (GO 6761; PI: S. Trammell). This camera has a field of view (FoV) of $40''\times 40''$ and a plate scale of $0''.05$ per pixel. Total exposure time was 5000 s. The continuum (V band) image was obtained with the ACS/HRC camera using the broad-band filter F606W ($\lambda_c=5907\text{\AA}$, FWHM=2342 \AA) on 2002-12-23 (GO 9463; PI: R. Sahai). The ACS camera has a field of view of $26''\times 29''$ and a plate scale of $0''.025$ per pixel. Total exposure time was 800 s. The images (Figs. 1 and 2) were pipeline reduced.

2.2. Optical Spectroscopy

We have obtained optical long-slit spectra of M2-56 using the Intermediate Dispersion Spectrograph (IDS) of the 2.5m Isaac Newton Telescope (INT) and the Andalucía Faint Object Spectrograph and Camera (ALFOSC) mounted on the 2.6 m Nordic Optical Telescope (NOT) of the Roque de los Muchachos Observatory (La Palma, Spain). Observations were performed in three different campaigns in 1998, 2000, and 2009. The log of our multi-epoch spectroscopic observations is given in Table 1.

2.2.1. *INT+IDS*

For the first set of spectroscopic observations with IDS (run#1), the detector used was a TEK $24\mu\text{m}$ CCD with 1124×1124 pixels mounted on the 500mm camera. Three slits positions were observed: one at position angle $PA=90^\circ$ (the symmetry axis of the nebula) passing through the nebula center (referred to as PA90) and two oriented along $PA=0^\circ$, one passing through the bright nebula center (PA0) and the other approximately through the

¹IRAF is distributed by the National Optical Astronomy Observatories, which are operated by the Association of Universities for Research in Astronomy, Inc., under cooperative agreement with the National Science Foundation.

center of the East lobe (at offset $\Delta\alpha\sim+6''$ from the center, PA0E) – see Fig. 3, leftmost panel. The slit was $1''$ wide and long enough to cover the whole nebula. CuNe lamps were used for wavelength calibration. The achieved spectral resolution (FWHM of the calibration lamp lines) was $\sim 44 \text{ km s}^{-1}$ around $\text{H}\alpha$.

For the second set of spectroscopic observations with IDS (run#2) the detector was the EEV10 CCD, with squared pixels of $13.5\mu\text{m}$ lateral size. Only a clear and unvignetted region of 700×2600 pixels was used (the 2600 pixels were along the spectral axis). The CCD was mounted on the 500mm camera. A total of four slits positions were observed with the R1200Y grating (Fig. 3, leftmost panel): we repeated positions PA90 and PA0E, already observed in run #1, and also added two more, one oriented along $\text{PA}=0^\circ$ passing through the West lobe (at offset $\Delta\alpha\sim-6''$ from the center, PA0W) and another one passing through the nebula center but oriented along $\text{PA}=119^\circ$ (PA119). For the slit position PA90 we also observed with the R900V grating. We used CuNe and CuAr lamps to perform the wavelength calibration. The spectral resolution achieved was $\sim 50 \text{ km s}^{-1}$, at $\text{H}\alpha$, and $\sim 83 \text{ km s}^{-1}$, at $\text{H}\beta$.

In both runs, #1 and #2, flux calibration was done using sensitivity functions derived from spectrophotometric standards, namely, HR1544, HR3454, and HD217086, and taking into account the atmospheric extinction curve at La Palma. All observations were performed under photometric conditions and with a typical seeing of $\sim 1''$ except for those carried out the first night of our run #2 (2000-11-11), during which an average seeing of $\sim 2''$ was measured. A secondary flux calibration of the mentioned dataset observed under non-photometric conditions (i.e. within the $\sim 6200\text{-}6800\text{\AA}$ range covered by grating R1200Y) was performed by matching the fluxes of the $[\text{S II}]\lambda\lambda 6716, 6731\text{\AA}$ doublet lines measured in 1998 and 2000, that is, assuming that the line fluxes have not changed with time. This is a reasonable assumption given the stability of the profile of these lines in all our campaigns (including run #3 in 2009). We derive a value for the scale factor of ~ 4 ($F_{2000}^{[\text{SII}]} \times 4 \sim F_{1998}^{[\text{SII}]}$). Once applied to all line fluxes in the range $6300\text{-}6740\text{\AA}$, this factor also corrects for the different seeing in our non-photometric data ($\sim 2''$), which affects the fraction of the nebular emission that enters the slit. We double-checked the obtained flux scale factor by comparing the fluxes integrated over the nebular core (the inner $\sim 2''$) of all lines (not only $[\text{S II}]$) in the spectra taken in 2000 along PA90 (under non-photometric conditions) and along PA119 (under photometric conditions), since both slits pass through almost the same central regions.

The data were reduced using standard procedures for long-slit spectroscopy within the IRAF package. The long-slit spectra presented in Figs. 3 and 4 have been smoothed with a flat-topped rectangular kernel of dimension 3×3 pixels to increase the S/N.

2.2.2. NOT+ALFOSC

Observations were done in service time mode using the CCD #8 detector, with 2048×2048 $13.5 \mu\text{m}$ sized pixels, and the VPH Grism #17. A $0''.9$ -wide ($5''.3$ -long) slit oriented at $\text{PA}=90^\circ$ and passing through the nebula center (slit $\text{PA}90$) was employed. The effective spatial resolution (seeing) was $0''.9$. We observed and used Ne lamps for wavelength calibration. The achieved spectral resolution $\sim 61 \text{ km s}^{-1}$ around $\text{H}\alpha$. The spectrophotometric standard star BD+284211 was observed and used for primary flux calibration. A secondary flux scale factor of ~ 7 has been obtained, following the procedure described in the previous subsection 2.2.1, and applied to the data. Final spectra, obtained after standard data reduction with IRAF, are shown in Figs. 5-7.

3. Results

3.1. Imaging

In Fig. 1 we present images of M 2-56 that unveil the different components of the optical nebula and their morphology. We find two pairs of nested lobes similarly oriented in the plane of the sky (along P.A. $\sim 90^\circ$) but with different sizes and a large contrast in surface brightness. The bright inner lobes (ILs), which can only be identified and spatially resolved in the *HST* images, have an angular size of $\sim 1''.5 \times 1''$ and display closed, bow-like ends, which very likely represent shock fronts. A 'three finger'-like structure at the base of the east IL (within $0''.5$ from the core) can be seen in the F606W image. The faint, more extended ($\sim 13'' \times 10''$), outer lobes (OLs), which are probed by our deep ground-based images but are only barely detected in the *HST* images, enclose the inner ones. Both pairs of lobes present an overall axial symmetry, however, they display a remarkable clumpy structure, including strings of compact knots and curved features that do not always have an axial counterpart.

The surface brightness of the east lobes is larger than that of the west ones². This is most likely a result of a larger extinction of the west side of the nebula, which is receding from us, given the hourglass distribution of the molecular, and presumably dust, envelope around the optical nebula (§ 1 and § 5). The larger brightness contrast at the central parts of the nebula (e.g., note that the three-finger structure of the eIL does not have a counterpart in the west) is consistent with a larger extinction along the densest equatorial regions.

In spite of their different filter bandwidth, both the broad- and narrow-band *HST*

²Hereafter, we will refer to the east (west) ILs and OLs as eILs and eOLs (wILs and wOLS), respectively.

images of M2-56 trace approximately the same gas component, as deduced from our long-slit spectra (§3.2). First, the contribution of the continuum to the emission within the F606W and F656N filters was negligible at the time the *HST* images were acquired, except maybe in the innermost regions of the ILs (within $\pm 0''.25$) where a very weak continuum level is detected in our spectra. Second, although the broad-band filter F606W includes several lines other than $H\alpha$, e.g., $[\text{N I}]\lambda 5200\text{\AA}$, $\text{Na I}\lambda 5893\text{\AA}$, $[\text{O I}]\lambda\lambda 6300, 6363\text{\AA}$, $[\text{N II}]\lambda\lambda 6548, 6583\text{\AA}$ and $[\text{S II}]\lambda\lambda 6717, 6731\text{\AA}$ (see also G91), the majority of these low-excitation transitions are expected to arise in the same $H\alpha$ -emitting regions probed by the F656N filter. The only exception could be the $[\text{N II}]$ and $[\text{S II}]$ doublets, which may proceed from regions with a slightly higher excitation, however, these lines have a contribution to the total line flux within the F606W filter of less than 30% (see Table 2 and G91).

We have noticed some differences between the two *HST* images, F656N and F606W, which were observed in 1998 and 2002, respectively. In particular, the string of knots/clumps at the tips of the ILs in 2002 is located $\approx 0''.10$ - $0''.16$ ahead the same structure as it was observed in 1998 (Fig. 2). This is true for both the east and west ILs and we believe it is due to proper motions³ ($\Delta\theta_t \sim 0''.03 \text{ yr}^{-1}$) resulting from the fast expansion of the ILs (see §3.2.1 and 4.1).

The base of the eIL also has a quite different appearance in the F606W and F656N images. In particular, the three finger-like structure visible in the F606W image is absent in the F656N image. In the latter image, the same region, i.e. the base of the eIL, shows an asymmetrical cone-like morphology but has a smoother brightness distribution slightly elongated to the north-east. These changes cannot be unambiguously attributed to real variations with time of the nebular structure since we cannot rule out some contribution from continuum emission (due to dust scattering in these innermost regions) that may be different in the F656N and F606W filters.

Finally, we have compared our two-epoch $H\alpha$ images observed with the *HST* in 1998 and with the INT in 2009. There is an emission clump located at offset $\Delta\alpha=5''$, $\Delta\delta=8''$ that is visible in both data sets (clump C1; Fig. 1). Surprisingly, there is another pair of even brighter clumps in the ground-based image, labeled C2 and C3, which are not detected in the *HST* images. Other fainter clumps or knots within the OLs (e.g. C3') visible in our 2009 images may have remained below the noise level in the *HST* images.

³Here the term "proper motion" is not used to describe the apparent motion of the nebula as a whole with respect to more distant stars but to refer to the tangential motion of material in the expanding nebula (e.g. the knots).

3.2. Spectroscopy

In this section, we show the results from our multi-epoch spectroscopic observations. In Table 2 we report the fluxes (F_λ) of the different lines detected. These fluxes have been measured from the PA90 spectrum integrating along the 1''-wide slit and over the full width of the spectral profile, after fitting and subtracting the continuum level. In the table, we also provide dereddened fluxes (I_λ) for a mean logarithmic extinction coefficient of $c(\text{H}\beta)=1.5\pm 0.1$ (see §5).

We have discovered significant changes with time in the line and continuum emission spectrum of M 2-56. Amongst the different lines detected, $\text{H}\alpha$ is the transition displaying the most extreme profile variations. We will first report our results obtained from the spectra observed in 1998 and 2000, for which the differences found only affect the line emission from the nuclear regions. Next, we will describe the long-slit spectrum along PA90 obtained in 2009, which shows additional changes with respect to the data obtained in our two previous runs.

3.2.1. 1998 and 2000 observations

In Figs. 3 and 4, we show the optical spectrum of M 2-56, which is composed of recombination and forbidden line emission plus a weak, red continuum. In 1998, the continuum emission arises from a central compact region that is unresolved in our data (with a $\text{PSF}\sim 0''.9$). The continuum intensity near $\text{H}\alpha$ (around 6510\AA) in 1998 integrated over the $1''\times 1''$ central region of M 2-56 is $\sim 1.5(\pm 0.4)\times 10^{-17}\text{ erg s}^{-1}\text{ cm}^{-2}\text{ \AA}^{-1}$. In 2000, we derive an upper limit for the continuum intensity within the same central region of $< 2.4\times 10^{-17}\text{ erg s}^{-1}\text{ cm}^{-2}\text{ \AA}^{-1}$ (i.e. $< 2\sigma$). Therefore, the non detection of the continuum in 2000 is consistent with its intensity remaining constant from 1998 to 2000. (As shown in §3.2.2, the continuum is brighter in 2009).

The long-slit $\text{H}\alpha$ spectrum is characterized by a wide profile with a quite complex spectral and spatial distribution (Fig. 3). Along the nebula axis (slit PA90), the $\text{H}\alpha$ emission can be traced from the brightest central regions up to the fainter tips of the OLS at $\pm 12''$. The $\text{H}\alpha$ emission from the east and west lobes (approaching to and receding from us, respectively, §1) is, on average, blue- and red-shifted, consistent with an expansive nebular kinematics. The spatial distribution of the emission from the bright, compact ILS is only partially resolved in our long-slit spectra and can be traced from the center up to $\pm 2''$. In these innermost regions, the much fainter OLS are not expected to contribute significantly to the $\text{H}\alpha$ emission given the large brightness contrast with the ILS evidenced by the *HST* images. Along the ILS,

the line-of-sight or radial expansion velocity increases with the distance reaching a maximum value of $V_r = V_{\text{LSR}} - V_{\text{sys}} \sim 110 \text{ km s}^{-1}$ at the tips. In these outermost regions of the ILs, the $\text{H}\alpha$ profile is rather broad, with a full width at zero intensity (FWZI) of $\sim 360 \text{ km s}^{-1}$. The $\text{H}\alpha$ long-slit profile along and across the OLs (e.g., along PA0E) is roughly consistent with the lobes being expanding bubble-like structures. We measure a value for the mean radial expansion velocity of the OLs of $V_r \sim 50 \text{ km s}^{-1}$, which is smaller than that derived for the ILs. In the outermost parts of the OLs, at axial offsets $\pm 10''\text{-}12''$ (PA90), our spectra indicate a slightly smaller radial expansion velocity of $V_r = 30\text{-}35 \text{ km s}^{-1}$.

We have found remarkable differences between the $\text{H}\alpha$ emission from the nucleus of M2-56 as observed in 1998 and in 2000 (Fig. 3). In 1998: a) the $\text{H}\alpha$ profile shows emission wings that are much broader (FWZI $\sim 1000 \text{ km s}^{-1}$) than in 2000 (FWZI $\sim 450\text{-}500 \text{ km s}^{-1}$) – this difference is not explained by the lower S/N achieved in 2000 (note that the fainter emission from the OLs is well probed in our 2000 spectrum); and b) the $\text{H}\alpha$ emission peak is blue-shifted by $\sim 110 \text{ km s}^{-1}$ from the systemic velocity, unlike the spectrum in 2000, which peaks at V_{sys} . We refer to the intense, blue-shifted emission feature and its broad wings observed in 1998 as feature F1. We have checked that feature F1 was not present either in the long-slit spectrum along the nebula axis acquired in 1989 by G91. The broad wings of feature F1 are not symmetric, the blue wing seems to be depressed relative to the red one, which may be interpreted as a blue-shifted (P-Cygni like) absorption in the profile. The blue-shift of the wing absorption is found at $V_r \sim -430 \text{ km s}^{-1}$. The presence of the spectral component F1 is clearly appreciated also in the $\text{H}\alpha$ spectrum taken with the slit oriented along the nebula equator PA0. The angular size of the region that produces feature F1 is very small, $\sim 0''.5$ along the main symmetry axis of the nebula and unresolved along the equator ($< 0''.6$).

In 1998, feature F1 was not only visible in the $\text{H}\alpha$ spectrum but also in the $[\text{N II}]\lambda\lambda 6548, 6584\text{\AA}$ lines. In contrast, feature F1 is not present in the $[\text{S II}]\lambda\lambda 6716, 6732\text{\AA}$ transitions: note that the two lines of the doublet have comparable profiles in 1998 and 2000 (see Fig. 7). The profiles of the $[\text{S II}]$ lines are indeed very much alike to those of $\text{H}\alpha$ and the rest of the transitions as observed in 2000 (and in 2009, see next subsection § 3.2.2).

3.2.2. 2009 observations

Figs. 5 and 6 display the long-slit spectrum of M2-56 obtained in 2009. Multi-epoch spectra extracted over the central $1'' \times 1''$ region are compared in Fig. 7.

In 2009, a relatively faint, red continuum is observed not only at the center (as in 1998)

but also along the lobes of M 2-56. As for most pPNs, the continuum emission is dominated by the stellar photospheric continuum scattered off by the nebular dust (we have checked that the contribution by nebular continuum is negligible given the intensity of the H α emission). The spatial distribution of the scattered continuum peaks at the nebula center and has two relative maxima at axial offsets $\pm 6''.5$. The latter regions correspond to condensations C3 and C3' in the ground-based images (Fig. 1). The central region where the continuum is observed has a deconvolved angular size along the axis of $\sim 1''.5$, i.e. significantly larger than in 1998 ($< 0''.5$). The continuum flux near H α (around 6510\AA) within the $1'' \times 1''$ central region in 2009 is $\sim 3.2 \times 10^{-16} \text{ erg s}^{-1} \text{ cm}^{-2} \text{ \AA}^{-1}$, that is, larger than that measured in 1998 by a factor ~ 20 .

The shape of the H α long-slit profile shows marked differences with respect to that observed earlier, not only in the central regions but also along the extended OLs. The H α emission from both the approaching and receding (west and east, respectively) lobes is on average red-shifted, in contrast to what we observed in 1998 and 2000. The red-shift of the H α emission from the approaching eOL is smaller than that from the receding wOL. At the nebula center, the H α emission has a broad asymmetric profile that peaks at $V_{\text{LSR}} = 65 \text{ km s}^{-1}$, i.e. red-shifted (by $\sim 90 \text{ km s}^{-1}$) with respect to V_{sys} . The FWZI of the H α nuclear profile cannot be accurately determined because of blending with the adjacent [N II] doublet; we estimate that it is larger than 1300 km s^{-1} and probably reaches up to 2500 km s^{-1} .

The observed red-shift of the H α line for both the approaching and receding lobes indicates that in 2009 a significant fraction of the H α emission in the lobes is scattered, i.e. is not locally produced in the lobes but rather arises at the nebular core and is reflected by the nebular dust. In fact, the similar spatial distribution of the H α emission and the reflected continuum beyond $\pm 6''$ indicates that in these regions the H α emission is mainly scattered. In the inner regions, however, some contribution of unscattered H α emission (produced locally in the lobes) can still be appreciated. Composite H α line profiles consisting of two components (scattered and unscattered) are also found in other pPNs, for example, M 1-92 (Trammell et al. 1993), M 2-9 (Solf 2000), CRL 618 (Trammell et al. 1993; Sánchez Contreras et al. 2002), etc.

In contrast to H α , the long-slit profiles of the forbidden transitions [O I] $\lambda 6363\text{\AA}$, the [N II] $\lambda\lambda 6545, 6584\text{\AA}$ and [S II] $\lambda\lambda 6716, 6731\text{\AA}$ in 2009 are totally consistent with those observed in our previous runs⁴: roughly point-symmetric with respect to the spatial origin and V_{sys} and with the emission from the east and west lobes blue- and red-shifted, respectively. This is consistent with the forbidden lines being predominantly produced locally in the shocked

⁴Except for the presence of feature F1 in the [N II] doublet lines in 1998, § 3.2.1

nebular material.

We have discovered a number of emission lines in this work, including several Fe II, Fe I, and Si II permitted transitions (Fig. 5 and Table 2). We have also detected a broad (FWHM $\sim 6\text{\AA}$) absorption feature centered near 6673\AA at the nebula center but slightly blue-shifted, near 6670\AA , along the east and west lobes. The relative blue-shift of the band between the center and the lobes indicates that it does not have an interstellar or telluric origin but rather is associated to M 2-56. We have not found a satisfactory identification for this broad absorption, which may be a solid state or ice feature given its large width; a blend of atomic lines cannot be ruled out either.

The emission distribution of the recombination lines discovered is quite different from that of the forbidden transitions. As for $H\alpha$, the former are red-shifted with respect to V_{sys} along the approaching eOL as well as at the nebula center (these transitions are not detected in the fainter west lobes). The red-shift measured in the eOL is smaller than that in the center. We conclude that the observed recombination lines most likely arise at the nebula nucleus and their emission is scattered by circumstellar dust.

Another important change detected in 2009 is the increase of the relative intensity of $H\alpha$ with respect to the various forbidden transitions observed. For example, in 2009, the $H\alpha$ -to- $[\text{N II}]\lambda 6584\text{\AA}$ intensity ratio reaches a value of ~ 15 , much larger than in earlier epochs, ~ 3.2 - 3.4 . The large $H\alpha$ -to- $[\text{N II}]\lambda 6584\text{\AA}$ intensity ratio is consistent with the presence of a compact H II region at the heart of M 2-56 responsible for the extra $H\alpha$ flux in 2009: note the brightening of the $H\alpha$ line by a factor ≈ 10 relative to the flux measured in 2000.

4. Nebular components and their spatio-kinematic structure

In this section we describe the main nebular components in M 2-56 revealed by our data and analyze their spatio-kinematical structure. We also estimate the inclination of the nebula axis, which is a critical parameter to correct for projection effects both in the geometry and expansion velocities observed.

4.1. The inclination of the nebula

The inclination of the nebula axis is derived in two different ways. First, from the proper motions observed in the *HST* images (Fig. 2 and § 3.1). For a distance to M 2-56 of $d=2.1$ kpc (§ 1), the observed proper motions ($\Delta\theta_t\sim 0''.03\text{ yr}^{-1}$) imply a tangential expansion velocity (i.e. projected on the plane of the sky) of $V_t\sim 325\text{ km s}^{-1}$. Since the line-of-sight or radial velocity

at the tips of the lobes measured from our long-slit spectra is $V_r \sim 110 \text{ km s}^{-1}$ (§ 3.2), we obtain an inclination angle to the plane of the sky of $i = \tan^{-1}(V_r / V_t) = 19^\circ$. This value is in very good agreement with the independent estimate of $i = 17^\circ$ for the symmetry axis of the bipolar CO envelope by Castro-Carrizo et al. (2002). We derive an absolute (deprojected) expansion velocity at the tips of the ILs of $\sim 350 \text{ km s}^{-1}$. This value is similar to the FWZI of H α emission at the ends of the ILs; the latter is known to be a reliable indicator of the shock velocity for bow-type shocks, independent of orientation angle, preshock density, bow shock shape, and preshock ionization stage (Hartigan et al. 1987).

An independent estimate of i can be obtained from the radial velocities measured at clumps C3 and C3' in the east and west OLs, respectively, where the H α emission is mainly scattered (§ 3.2.2). Assuming that regions C3, C3', and the nebula center are aligned along a given axis, which is inclined to the plane of the sky by i , and that the clumps move away from the central star at the same expansion velocity, V_{exp} , then we can readily find V_{exp} and i from the following expressions:

$$V_{\text{exp}} = \frac{V_r(\text{C3}) + V_r(\text{C3}')}{2} \quad (1)$$

$$\sin(i) = \frac{[V_r(\text{C3}') - V_r(\text{C3})]}{[V_r(\text{C3}') + V_r(\text{C3})]} \quad (2)$$

(see, for example, Solf 2000). Taking into account the values of $V_r(\text{C3}) = 31.3 \text{ km s}^{-1}$ and $V_r(\text{C3}') = 60.9 \text{ km s}^{-1}$ measured on the H α spectrum along PA90 (Fig. 6), we obtain $V_{\text{exp}} = 46 \text{ km s}^{-1}$ and $i = 18.8^\circ$. The value of i found is in excellent agreement with that computed for the ILs from the proper motions and that of the bipolar molecular envelope.

4.2. Spatio-kinematic model of OLs and ILs

In order to investigate the structure and velocity field of the optical lobes of M 2-56 we have developed a simple spatio-kinematical model that reproduces the 2D profile of our long-slit spectra. Although the model has been mainly applied to the PA90 spectrum, we have checked that it also qualitatively explains the spectra at the other slit orientations. Our model calculates the position-velocity (p-v) diagram assuming a certain morphology for the envelope (compatible with our direct images) and a given velocity field, and also taking into account the inclination of the nebula to the plane of the sky ($i = 18^\circ$). We note that our

code is not an emission model, that is, does not predict the $H\alpha$ brightness distribution along PA90.

In Fig. 8 we present the geometry adopted and synthetic p-v diagrams predicted by our best model for the $H\alpha$ line. The nebular component responsible for the spectral feature F1 is not included in our model because it is not spatially resolved in our spectra. We are assuming in our model that the lobes are hollow and show an overall axial symmetry, as suggested by the optical appearance of M 2-56. For the OLs and the ILs, the model fit yields a linear size of about $(4 \times 10^{17} \text{ cm}) \times (3 \times 10^{17} \text{ cm})$ and $(6 \times 10^{16} \text{ cm}) \times (4 \times 10^{16} \text{ cm})$, respectively, measured along the symmetry axis and the perpendicular direction where the lobes reach their maximum extension.

For the adopted geometry, the velocity field that best reproduces the long-slit spectrum of the OLs consists of three main components: 1) radial expansion with the modulus of the velocity at each point increasing linearly with the distance to the nebula center; 2) axial expansion with the velocity modulus increasing linearly with the distance to the equatorial plane; and 3) shear-flow kinematics, with the velocity vectors tangential to the curved surface adopted for the lobes and with a constant velocity modulus. The components that dominate the velocity field in M 2-56 vary from the base of the OLs, where components 1) and 3) prevail, to the external regions, where the velocity field is essentially axial. The velocity field described above, with the flow speed increasing with the distance to the center, works fine for most parts in the OLs, however, is not able to reproduce the relatively low radial velocities measured at the tips, $\sim 110 \text{ km s}^{-1}$ around $\pm 10\text{-}12''$, which implies an abrupt slow down of the flow. In these outer regions, represented in our model as bow-shaped caps detached from the main body of the OLs, the expansion seems to be dominated by a constant velocity axial field.

Since the spatial structure of the ILs is only partially resolved in our 2D spectra, we have adopted a simple axial velocity field that is able to reproduce the overall velocity gradient observed within the inner $\pm 2''$. We deduce a rather steep variation of the deprojected expansion speed, increasing from tens of km s^{-1} near the center to $\sim 350 \text{ km s}^{-1}$ at the lobe tips.

4.3. The wind responsible for the transient $H\alpha$ feature F1

We believe that the $H\alpha$ emission burst observed in 1998, referred to as feature F1, is the consequence of a fast, dense, and short-lived post-AGB wind recently ejected (§ 7). We have measured a total angular size along the nebula axis of the region emitting feature

F1 of $\sim 0''.5$ (1.57×10^{16} cm). The spectral profile of F1, notably asymmetrical, peaks at $V_r \sim 110 \text{ km s}^{-1}$, i.e. bluewards of V_{sys} . This is consistent with a compact bipolar flow oriented similarly to the ILs and OLs, the red-shifted emission from the receding (west) side of the F1-wind being significantly extinguished by the optically thick equatorial regions of M 2-56. A larger extinction towards the inner regions of the wIL (compared to the base of the eIL) is, in fact, inferred from the brightness contrast between these two regions observed in the *HST* images and is also expected from the equatorially enhanced density distribution of the molecular envelope that surrounds the optical nebula of M 2-56 (§ 1 and § 5). (A one-sided collimated F1-wind is not impossible but improbable given the bipolar morphology, approximately symmetric with respect to the equator, of the optical and CO envelopes of M 2-56). Adopting a bipolar flow with an inclination to the plane of the sky of $i=18^\circ$, we obtain a linear extension for this component of $l_{\text{F1}} \sim 1.65 \times 10^{16}$ cm. The blue-shift of the intensity peak of F1 indicates that the bulk of the material in the F1-wind expands at a mean velocity of $V_{\text{exp}} \sim 110/\sin(18^\circ) \sim 360 \text{ km s}^{-1}$, very similar to the expansion speed at the tips of the ILs. The broad wings of feature F1 and the blue-shift (P-cygni like) absorption of the nuclear $\text{H}\alpha$ profile indicate smaller amounts of gas expanding at larger velocities (up to $\sim 500 \text{ km s}^{-1}$) in the F1-wind.

4.4. The central H II region

The presence of a compact H II region around the central star of M 2-56 is inferred from our data (§ 3.2.2). In 2009, a fraction of the $\text{H}\alpha$ emission from such a region escapes the stellar vicinity and reaches the ILs and OLs where it is scattered off by dust. The kinematics of the H II region cannot be straightforwardly determined from the $\text{H}\alpha$ line profile since the emission from this region is seen only after being reflected by the nebular dust, the resulting line profile being significantly affected by the distribution and kinematics of the dust. The broad profile of the $\text{H}\alpha$ emission from the nebula nucleus ($\text{FWZI} > 1900\text{-}2500 \text{ km s}^{-1}$) may indicate rapidly outflowing material in the stellar neighborhood, with very large expansion velocities of up to $\approx 1200 \text{ km s}^{-1}$, however, we cannot rule out other line broadening mechanisms (e.g., Ramman scattering) being totally or partially responsible for the large FWZI of the $\text{H}\alpha$ transition (see e.g. Sánchez Contreras et al. 2008, and references therein).

The $\text{H}\alpha$ scattered profile observed at C3' and C3 represents the profile emitted by the H II region as seen from the dust clumps located at those positions, i.e. from a "pole-on" view. As we can see in Fig. 6, the $\text{H}\alpha$ profiles at C3 and C3' are very similar (except for an overall relative red-shift of $30\text{-}40 \text{ km s}^{-1}$): they have a narrow intense core plus broad wings

and show a notable P-cygni like profile, with the blue side depressed. The $H\alpha$ emission towards the center exposes the profile emitted by the H II region as seen along the line-of-sight, i.e. from a direction nearly perpendicular to the lobes. Its overall red-shift indicates a significant contribution of scattered $H\alpha$ emission also towards the nebula center. In this direction, the $H\alpha$ profile is broader than that observed towards clumps C3 and C3' and does not exhibit prominent blue-shifted absorption. This suggests that the P-cygni like absorption observed at C3 and C3' is produced by neutral or partially neutral material outside the H II region and very likely distributed in a bipolar flow.

5. Extinction

We have used the $H\alpha$ to $H\beta$ flux ratio measured in 2000 (Table 2) to estimate the extinction in M 2-56. Since the $H\alpha$ and $H\beta$ fluxes have been obtained integrating spatially the spectrum along slit PA90 over the whole nebula, the value derived represents an average of the extinction along the lobes, which is expected to decrease from the center (nebular equator) to the tips of the lobes. We have measured a Balmer decrement of $H\alpha/H\beta \sim 12 \pm 1$, for which we obtain a logarithmic extinction coefficient $c(H\beta) = 1.5 \pm 0.1$ adopting an intrinsic ratio $H\alpha/H\beta \sim 3.8$. The latter value of the intrinsic $H\alpha/H\beta$ ratio is expected for the shock-excitation conditions in M 2-56 derived by several authors comparing observational line relative intensities with the predictions of theoretical shock excitation models (Goodrich 1991; Trammell et al. 1993; Riera et al. 2006, and references therein). (For an intrinsic Balmer decrement closer to the recombination value, $H\alpha/H\beta \sim 3$, we obtain $c(H\beta) = 1.7-2.0$.) From the value of $c(H\beta)$, we deduce an average optical depth near $H\alpha$ (around 6563\AA) of $\tau_{6563} \sim 2.3$ and, therefore, an average extinction in the V band of $A_V \sim 3$ mag, using the extinction law parametrization by Cardelli et al. (1989) and assuming the ratio of total to selective absorption, R_V , equal to 3.1. Our result is in good agreement with previous estimates of $A_V = 3.3$ and 4.8 mag (Goodrich 1991; Cohen & Kuhl 1977), especially taking into account the lower intrinsic Balmer decrement, 3 and 2.85, adopted in these earlier works.

We have compared the extinction computed above with that predicted from the detailed model of the molecular envelope of M 2-56 performed by Castro-Carrizo et al. (2002) based on high-angular resolution interferometric maps of the CO ($J=1-0$ and $J=2-1$) emission. The molecular envelope surrounds the optical nebula and is expected to contain a mixture of gas and dust. We have derived the relative variation along the lobes of the CO column density from the geometry and density spatial distribution in the model. Adopting a given CO-to- H_2 relative abundance, $X(\text{CO})$, and the standard conversion factor from H_2 column density to optical extinction $N_{H_2} = 2.3 \times 10^{21} A_V \text{ cm}^{-2}$, we have calculated the relative variation of

the circumstellar extinction (A_V^{CS}) along the lobes produced by the dust in the hourglass-shaped molecular envelope (Fig. 9, left). In order to determine the total (circumstellar plus interstellar) extinction, we have added the interstellar contribution in the direction to M 2-56, which is $A_V^{\text{ISM}}=1.75$ according to the “Galactic Dust Reddening and Extinction” calculator provided by IRSA/IPAC⁵ (Fig. 9, right).

In their model, Castro-Carrizo et al. (2002) adopt a typical value of $X(\text{CO})=2\times 10^{-4}$, however, these authors affirm that the average CO abundance in this object must be substantially lower due to significant photodissociation of this molecule. We find that assuming $X(\text{CO})\approx 3\times 10^{-5}$ we are indeed able to reproduce very well the total extinction derived from the Balmer decrement. (Note that most of the $\text{H}\alpha$ and, especially, $\text{H}\beta$ emission arise in the bright ILs, therefore our estimate of $A_V\sim 3$ mag represents the mean extinction over the central $\pm 2''$ - $3''$). We have obtained an independent estimate of $X(\text{CO})$ by comparing the total dust mass in M 2-56 obtained from simple SED modeling, $M_{\text{dust}}=1.5\times 10^{-3} M_{\odot}$, with the mass of the molecular envelope derived from CO, $M_{\text{gas}}=0.05 M_{\odot}$, assuming the standard value of $X(\text{CO})=2\times 10^{-4}$. Both masses are related by the following expression:

$$M_{\text{gas}} = M_{\text{dust}} \times \left[\frac{X(\text{CO})}{2 \times 10^{-4}} \right] \times \delta, \quad (3)$$

where δ is the gas-to-dust mass ratio, which is typically in the range $\delta=100$ - 200 in pPNs. Applying the previous equation, we deduce an average CO abundance of $X(\text{CO})\sim(3.3$ - $6.6)\times 10^{-5}$, comparable to that inferred from the extinction and the CO model explained above.

5.1. A compact, dusty “cocoon” around the star?

We have estimated the total optical extinction along the line-of-sight towards the central star of M 2-56 (A_V^{\star}) from the ratio between the continuum flux observed at a given wavelength (F_{λ}^{obs}) and that expected from the central star in the absence of absorption (F_{λ}). We compute F_{λ}^{obs} from the observed surface brightness at the nebula center and taking into account the PSF in our observations. On the other hand, F_{λ} has been approximated by the flux (measured on earth) emitted by a black body with an effective temperature of $T_{\text{eff}}=25,000$ K, a total bolometric luminosity of $L=5500 L_{\odot}$, and a distance to M 2-56 of $d=2.1$ kpc (§ 1). Considering the values obtained for $F_{6510}^{\text{obs}}=1.8\times 10^{-17}$ ergs⁻¹ cm⁻² Å⁻¹ and

⁵<http://irsa.ipac.caltech.edu/applications/DUST/>

$F_{6510}=4\times 10^{-13}\text{ erg s}^{-1}\text{ cm}^{-2}\text{ \AA}^{-1}$, we infer a value for the total extinction towards the star of $A_V^*=12\text{ mag}$. The slope of the continuum emission over the whole wavelength range observed by us in 1998 is indeed very well matched by that predicted by the reddened black body above. The color of the continuum, however, is not compatible with a lower value of $A_V^*\sim A_V\sim 3\text{-}4\text{ mag}$ since, in that case, the central star would have to be unreasonably hot ($T_{\text{eff}}\gtrsim 300,000\text{ K}$), which is totally in contradiction with the low-excitation conditions and lack of substantial photoionization of the optical nebula of M 2-56.

Our value of A_V^* is significantly larger than the average nebular extinction implied by the Balmer decrement and also larger than the maximum value deduced from the CO column density under a reasonable assumption of the CO abundance (see §5). This result is not totally unexpected: the CO model only accounts for the extinction produced by the extended hourglass-like envelope that surrounds the optical lobes, where the $H\alpha$ and $H\beta$ emission is locally produced, but does not include the possible attenuation of the stellar radiation produced by a potential/conceivable dusty structure *inside* the optical lobes and closer to the stellar surface. The absence of scattered continuum along the lobes in 1998 suggests that the light from the star was largely attenuated in that epoch not only along the line-of-sight, as indicated by the large A_V^* found, but also along the nebular symmetry axis, i.e. in the direction to the lobes. It is then quite plausible that the structure responsible for the large optical depth towards the star was completely (or almost completely) surrounding the latter in 1998 forming, for example, a dusty "cocoon" or shell. Since such a cocoon or shell-like obscuring structure is most likely surrounding the close stellar environment and, thus, deep inside the ILs, we derive an upper limit to its radius of <0.1 ($<200\text{ AU}$) from the PSF of our high-angular resolution *HST* images.

5.2. Recent decrease of the optical depth towards the star

The remarkable spectral differences observed in 2009 with respect to 1998 and 2000 (§3.2.2) signal important physical changes at the core of M 2-56. On the one hand, the recent appearance in 2009 of scattered continuum all along the lobes suggests that: 1) the intrinsic intensity of the stellar continuum has increased; and/or 2) the optical depth of the material (cocoon?) around the star has decreased (at least in the direction to the lobes) leading to a larger fraction of the stellar radiation to escape and to reach the lobes where it is reflected by the dust. This (option 2) would also explain the increment of the scattered (versus locally produced) $H\alpha$ emission along the lobes in 2009 and, in particular, the recent brightening of clumps C3 and C3' evidenced by the direct images (Fig. 1). On the other hand, we have observed a significant brightening of the continuum between 1998 and 2009.

In particular, at the nebula center we measure $F_{6510}^{\text{obs}}(2009) \sim 15 \times F_{6510}^{\text{obs}}(1998)$. We believe that a true variation of the luminosity or the stellar temperature is very unlikely to be the cause of such brightening. First, an increase of the luminosity would be totally unexpected in the post-AGB phase, which is characterized by a progressive warming of the central star at constant luminosity. Second, only a decrease of the stellar temperature down to $T_{\text{eff}} \sim 5500\text{--}6000\text{ K}$ (at constant luminosity $L = 5500 L_{\odot}$) combined with an extinction of $A_V^* = 11.7\text{ mag}$ would be able to reproduce the continuum spectrum observed in 2009. Such an extreme cooling of the star, however, would not only be unprecedented but, most importantly, would be inconsistent with a) the presence of a compact circumstellar H II region in 2009, which requires a relatively warm star ($T_{\text{eff}} \gtrsim 20,000\text{ K}$), and b) the lack of metallic absorption lines typical of a G-type star in the stellar spectrum of M 2-56.

Accordingly, the increase of scattered (continuum and H α) emission along the lobes and the brightening of the continuum at the center are both most likely due to a decrease of the optical depth of the circumstellar dust enshrouding the nebula's core (which includes the star and the compact circumstellar H II region).

Applying the same method and adopting the same value for F_{6510} as in § 5.1 and taking into account the continuum flux measured in 2009 near H α , $F_{6510}^{\text{obs}} = 2.7 \times 10^{-16}\text{ erg s}^{-1}\text{ cm}^{-2}\text{ \AA}^{-1}$ (§ 3.2.2) we deduce a value of $A_V^* = 8.8\text{ mag}$. Therefore we conclude that the extinction towards the star along the line-of-sight has decreased by $\sim 3\text{ mag}$ from 1998 to 2009.

We have also estimated a lower limit to the decrease of the optical depth from the star to the lobes, in particular, to the location of condensation C3 of the eOL (Figs. 1 and 5) from the ratio of the surface brightness of the scattered continuum at that point in 2009 and in 1998. The stellar scattered continuum observed at C3 is attenuated by *i*) the dust inside the lobes, i.e. from the star to C3 (symbolized as $\star \rightarrow \text{C3}$), and also by *ii*) the dust between C3 and us along the line-of-sight, i.e. contained in the extended CO envelope that surrounds the optical lobes and in the ISM. However, the extinction produced by the latter components is not expected to vary with time (at least, not in less than $\approx 10\text{ yr}$). In 1998, the continuum is not detected, therefore we use an upper limit given by the rms noise in our spectra ($1\sigma = 3.1 \times 10^{-18}\text{ erg s}^{-1}\text{ cm}^{-2}\text{ \AA}^{-1}\text{ pix}^{-1}$). In 2009, we measure $1.1 \times 10^{-17}\text{ erg s}^{-1}\text{ cm}^{-2}\text{ \AA}^{-1}\text{ pix}^{-1}$ at 6510 \AA . Therefore, we conclude that the extinction from the star in the direction to the lobes has decreased by $A_V^{\star \rightarrow \text{C3}} > 1.6\text{ mag}$ from 1998 to 2009.

6. Density and Nebular Mass

6.1. The electron density distribution

We have used the [S II] λ 6716/ λ 6731 doublet ratio to estimate the electron density, n_e , along the shocked lobes of M 2-56. In Fig. 10, we plot the spatial profiles along the nebula axis (slit PA90) for the two doublet lines and their ratio obtained from the spectrum observed in 2009 (with the highest S/N ratio and best spatial resolution amongst our multi-epoch data). We have checked that the ratios measured in 1998 and 2000 (not shown here) are roughly consistent with those obtained in 2009 within the observational errors.

The [S II] λ 6716/ λ 6731 ratio increases with the axial distance from the nebula center, which implies a decrease of n_e from the center to the outer parts of the lobes, considering the [S II] λ 6716/ λ 6731 ratio versus n_e relationship (e.g. Osterbrock & Ferland 2006) and adopting an average electron temperature $T_e = 10,000$ K consistent with the estimate by Cohen & Kuhi (1977); Trammell et al. (1993). We derive the largest value of $n_e > 2 \times 10^4 \text{ cm}^{-3}$ towards the nebula center (within the PSF, i.e. $\pm 0''.5$), where the high-density limit of the [S II] λ 6716/ λ 6731 ratio, ~ 0.4 , is reached. Along the ILS, n_e ranges between 2000 cm^{-3} , at the base ($\pm 0''.5$), and 1000 cm^{-3} , at the tips ($\pm 2''$). In the inner regions of the OLs (from $\pm 2''$ to $\pm 3''$), the density steeply varies between $\lesssim 1000$ and 500 cm^{-3} and then decreases down to 150 cm^{-3} at $\pm 5''$. Beyond these regions the OLs may become more tenuous, if the spatially decreasing trend of n_e is maintained, however, the large data errorbars prevent an accurate determination of the doublet ratio.

The p-v diagram of the two lines of the [S II] doublet and their intensity ratio, which are represented in Fig. 10, provides more details on the distribution of n_e in M 2-56. In particular, unveils the presence of a dense equatorial region at the center (approximately within $\pm 1''$) with a velocity gradient markedly different from (opposite to) that in the lobes. Such a velocity gradient is indicative of expansive motions in the direction perpendicular to the nebula symmetry axis. The velocity and the density along the equatorial flow are both found to increase with the distance to the center, reaching values of up to $\approx 100 \text{ km s}^{-1}$ and $\gtrsim 2 \times 10^4 \text{ cm}^{-3}$. (We cannot rule out a radial decrease of the electron temperature being totally or partially responsible for the radial decrease of the [S II] λ 6716/ λ 6731 ratio). The center of the expansion may be slightly bluewards of V_{sys} , at $V_r \sim -60 \text{ km s}^{-1}$.

Finally, we have estimated a lower limit to the density of the region/wind responsible for the transient feature F1 observed in the $H\alpha$ profile (and, to a lesser extent, the [N II] $\lambda\lambda$ 6548,6584Å doublet) in 1998. We believe that the most likely reason why feature F1 had vanished in 2000 is that the material ejected during the $H\alpha$ -emission burst had become fully (or almost fully) recombined in the time span between our runs #1 and #2, i.e. in

just 2.9 yr or less. This enables estimating a lower limit to the average density in the fast F1-wind in 1998 of $n_e \gtrsim 2.6 \times 10^4 \text{ cm}^{-3}$ using the expression for the recombination time scale, t_r , as a function of the density given by Kwok (2000): $t_r \sim 7.6 \times 10^4 / [n_e / \text{cm}^{-3}] \text{ yr}$. Such a value of the density, relatively high, is consistent with feature F1 not being present in the [S II] spectrum: given the critical density of the lines in the doublet these transitions would be significantly suppressed by collisional de-excitation in high-density regions. The lines of the [N II] doublet have larger critical densities, $n_c \sim \text{few} \times 10^4 \text{ cm}^{-3}$, that is why the F1-wind is traced by these transitions.

6.2. Atomic and Ionized Mass

We have estimated the total mass of atomic and ionized gas, M_{H} and M_{H^+} , in the lobes of M2-56 using the mean electron densities derived above and the total energy radiated by [O I] λ 6300 and H α , respectively. The [O I] (H α) intensity is proportional to the product of n_e and the H (H $^+$) number density, assuming that the transitions are optically thin and that the electron temperature does not strongly vary within the emitting region. Considering a mean electron temperature in the shocked lobes of $T_e = 10,000 \text{ K}$ (Cohen & Kuhi 1977; Trammell et al. 1993), relative abundances of He/H = 0.1 and O/H = 4×10^{-4} and the required atomic parameters (see e.g. Mendoza 1983; Gurzadyan 1997) we derive:

$$M_{\text{H}}^{[\text{OI}]}(M_{\odot}) = 7.7 \times 10^{-5} \left(\frac{n_e}{10^4 \text{ cm}^{-3}} \right)^{-1} \left(\frac{L_{[\text{OI}]}}{0.1 L_{\odot}} \right), \quad (4)$$

$$M_{\text{H}^+}^{\text{H}\alpha}(M_{\odot}) = 9.6 \times 10^{-5} \left(\frac{n_e}{10^4 \text{ cm}^{-3}} \right)^{-1} \left(\frac{L_{\text{H}\alpha}}{0.1 L_{\odot}} \right), \quad (5)$$

where L is the dereddened luminosity of the line (and we have adopted $d = 2100 \text{ pc}$). Note that Eq. (4) is valid for electron densities smaller than the critical density of [O I], $n_c \sim 10^6 \text{ cm}^{-3}$, which is the case for M2-56. On the other hand, this equation only provides a lower limit of the total atomic mass (M_{H} , which includes the He contribution), since we are assuming that most of the oxygen is neutral and in the ground state. Also, we note the dependence of the mass derived using Eq. (4) on T_e as $M_{\text{H}}^{[\text{OI}]} \propto \sqrt{T_e} / (e^{-2.3e4/T_e})$. In deriving Eq. (5) we have assumed that the majority of the electrons in the nebula come from H $^+$, i.e., $n_e \sim n_{\text{H}^+}$, and the classic radiative recombination case b for $T_e \sim 10,000 \text{ K}$ (i.e. $z_3 = n_3 / n_e n_{\text{H}^+} = 0.25 \times 10^{-20} \text{ cm}^3$, where n_3 is the population of the level $n = 3$ of H; Gurzadyan 1997).

We have separately estimated the masses of the OLs and ILs using the line fluxes integrated within each component and using Eqs. (4) and (5). We have also estimated M_{H^+} in the F1-wind calculating the flux in the feature F1 computed as the difference between the $\text{H}\alpha$ fluxes measured in 1998 and 2000. To derive the total mass in the extended OLs we have used the fluxes in Table 3 multiplied by a factor ~ 3 , which converts the flux within a $1''$ -wide slit to total nebular flux (estimated from the direct *HST* and ground-based images, Fig.1). We assume, however, that the compact ILs and wind-F1 lie completely within our $1''$ -wide slit. Our results are given in Table 3 together with the average values of the extinction and electron densities used for each nebular component (estimated in § 5 and § 6.1). For the F1-wind our value of the ionized mass is particularly uncertain since the density and the extinction are poorly known in this case. The extinction by which the flux in the F1 feature needs to be corrected for could be of up to ~ 12 , if it is extinguished similarly to the central star, or ~ 3 , if it is extinguished similarly to the ILs. Given the angular size of the F1-emitting region ($0''.5$), which is larger than that inferred for the cocoon around the nebula's core ($<0''.1$, § 5.1), we favor a moderate extinction (i.e. closer to ~ 3) for this component. Given the lower limit to n_e , we calculate an upper limit to the mass of the F1-wind of $<4 \times 10^{-6} M_{\odot}$.

We have also estimated the mass of ionized material in M 2-56 geometrically, using the mean electron densities and the volume of the shocked lobes directly measured from the images, assuming a simplistic spherical geometry for the lobes. We have separately considered the case of hollow lobes and lobes uniformly filled with gas. Assuming hollow lobes with $\sim 0''.2$ -thick walls, the ionized mass of the ILs and OLs is $\sim 7 \times 10^{-5} M_{\odot}$ and $\sim 6 \times 10^{-4} M_{\odot}$, respectively. These values are consistent with those previously obtained from the $\text{H}\alpha$ luminosity (Table 3). For the adopted values of the mean electron density and taking into account the limitations of our necessarily simplistic assumptions made to derive the mass, the thin-walled lobes scenario seems to be a better approximation to the structure of the lobes of M 2-56 than the filled-lobes geometry: for the latter, the derived masses systematically exceed those obtained from the $\text{H}\alpha$ luminosity. We note that the limb-brightening of the ILs and, to a lesser extent, the OLs observed in the images support the hypothesis of relatively thin-walled lobes.

7. Discussion: formation and evolution of M 2-56

We interpret the nebular morphology and kinematics of M 2-56 in the context of the AGB-to-post-AGB wind interaction scenario, i.e., resulting from the hydrodynamical interaction between fast, collimated (jet-like) post-AGB ejections and the slowly expanding

envelope expelled during the previous AGB phase (see §1). The remarkable “lobe inside a lobe” appearance of M2-56 together with the discovery of the recent $H\alpha$ emission burst, and the revelation of other very small-scale structures at the nebula’s core points to multiple episodes of mass outflow during the post-AGB phase.

The earliest post-AGB mass-loss event in M2-56 (that we have knowledge of from existing data) is probably the one that shaped and accelerated the extended hourglass-like molecular outflow enclosing the optical nebula (§1). As discussed by Castro-Carrizo et al. (2002), such an interaction started approximately ~ 1400 yr ago and took place quickly, in less than 300 yr (see also Bujarrabal et al. 2001). The smaller kinematical ages of the optical OLs and ILs derived from our long-slit spectra, $t_{\text{kin}} \sim 380$ and ~ 40 yr, respectively, suggest that the latter resulted from two consecutive and more recent post-AGB ejections. The duration of such ejections cannot be asserted based on our data but it may be a small fraction of their kinematical ages as in the case of the fast molecular outflow. We find that the caps of the optical OLs, which are located immediately behind of two diametrically opposed dense axial clumps traced by CO, show a different kinematics than the main body of the OLs. In particular, the OLs-caps are characterized by expansion velocities close to those of the aforementioned CO condensations. The kinematical age derived for the OLs-caps, $t_{\text{kin}} \sim 1200$ yr, is thus similar to that of the CO axial clumps, which may suggest that both were shaped and accelerated in the same wind interaction process between the primer post-AGB bipolar flow(s) and the AGB envelope. In this scenario, the massive molecular envelope would be mainly composed of shocked-AGB wind whereas the OLs-caps could be a remnant of the primer post-AGB wind. Alternatively, the material in the OLs-caps could have been ejected at the same time as the rest of the OLs, i.e. ~ 380 yr ago, and subsequently decelerated (from expansion speeds of $\sim 400 \text{ km s}^{-1}$ down to the observed velocities in these regions, $V_{\text{exp}} \sim 110 \text{ km s}^{-1}$) as a consequence of its interaction with the pre-existing CO clumps. The fast ILs probably trace a more recent shock interaction between an ensuing, fast post-AGB wind with the material at the base of the pre-existing and slower OLs.

Our data also uncover a dense equatorial structure at the nebula center that is expanding in the direction perpendicular to the lobes with radial velocities of up to $\sim 100 \text{ km s}^{-1}$ (§6.1 and Fig.10). The velocity gradient observed, which is approximately linear, indicates a kinematical age of ~ 300 -400 yr (adopting $i=90^\circ - 18^\circ = 72^\circ$). The similar age of the equatorial flow and the OLs is consistent with both components resulting from a single, sudden mass-ejection event that took place simultaneously along the nebula axis and in the perpendicular plane. This scenario has been proposed previously by Alcolea et al. (2007) to explain the radial acceleration along the equator and bipolar flows of the molecular envelope of the pPN M1-92. In M2-56, the compact equatorial structure unveiled by the [S II] doublet may represent the inner (warmer) regions of the dense, molecular ring/torus probed by CO

emission (§ 1). The lower expansion velocity of the latter ($V_{\text{exp}}=7\text{-}8\text{ km s}^{-1}$) may indicate substantial deceleration of the equatorial flow after interaction with the dense, slow AGB envelope. The density is found to increase outwards along the optical equatorial flow, in support of the presence of compressed (swept up) material at the boundary with the dense molecular torus.

The discovery of the $\text{H}\alpha$ emission burst from the nebular core in 1998 (feature F1) brings to light a latter stellar wind. As discussed in § 4.3, the F1-emitting wind is probably bipolar. The linear size and mean expansion velocity of this fast, compact flow allow us to derive an upper limit to its kinematical age of only $<14\text{ yr}$. The upper limit arises because of possible deceleration of the F1-wind by interaction with the ILs. The absence of feature F1 in the $\text{H}\alpha$ spectrum obtained in 1989 by G91, in fact, suggests that the F1 wind could have been ejected only $<10\text{ yr}$ before it was first identified in our run #1. In this case, the initial expansion speed of the F1-wind (before substantial deceleration took place) should have been $V_{\text{exp}}\sim 500\text{ km s}^{-1}$ to explain the axial extent of this component. This value of V_{exp} is indeed in agreement with that inferred from the broad wings and the P-cygni absorption component of feature F1, which indicate that a fraction of the F1-flow is actually moving at this relatively large speeds (§ 4.3).

The absence of feature F1 in 2000 is probably due to fast recombination of the gas in the dense ($>2.6\times 10^4\text{ cm}^{-3}$) F1-wind (§ 6.1). In order for the F1-wind to be completely or considerably neutral already in 2000, most of it should have been far away (detached) from the central star at that time, otherwise one would expect to observe emission from the dense photoionized material at the base of the wind close to the stellar surface as long as the wind is on-going. We conclude, therefore, that the rapid recombination observed, in less than $\sim 3\text{ yr}$, is most consistent with the F1-wind being a short-time duration event, e.g. a pulsed-jet or bullet-type ejection, leading to detached or clumpy structures, rather than being blown in a continuous way. We believe that the clumpy, jet-like structures observed in the direct *HST* images of M 2-56 at the base of the eIL could represent the footprints of such a fast F1-wind. This is based on the similar size and location of both structures in the images and the spectra. If this is correct, the emission that we see from the prominent three-finger like structure in the F606W *HST* image must be mainly stellar light *scattered* by the F1-wind, after recombination, since that image was obtained in 2002 once the $\text{H}\alpha$ emission feature F1 had disappeared.

We have estimated a lower limit to the mass-loss rate that led to the main nebular components identified in our optical imaging and spectroscopic data, namely, the OLs, the ILs and the F1-wind, from the ratio between the total mass contained in each component and their kinematical ages (Table 3). The lower limit arises because the duration of each of

the multiple post-AGB mass-loss episodes undergone by M 2-56 could be shorter than their kinematical ages. We obtain very similar values of the mass-loss rate for the OLs and ILs, namely, $\dot{M}_{\text{OLs}} \sim 2 \times 10^{-6}$ and $\dot{M}_{\text{ILs}} \sim 3 \times 10^{-6} M_{\odot} \text{ yr}^{-1}$. For the F1-wind, we compute a value of $\dot{M}_{\text{F1}} \sim 4 \times 10^{-7} M_{\odot} \text{ yr}^{-1}$, however, we note the larger uncertainties in this case mainly due to our vague estimate of the mass of the F1-wind. We have attempted a different estimate of the mass-loss rate of the F1-wind as given by $\dot{M} = \pi r_j^2 V_{\text{exp}} \rho$, where the geometry of the F1-wind is approximated by a cylindrical structure with radius r_j , density ρ , and expanding at V_{exp} . Adopting $r_j \sim 0''.05$, $\rho > 3 \times 10^4 \text{ cm}^{-3}$ and $V_{\text{exp}} \sim 500 \text{ km s}^{-1}$, we derive $\dot{M}_{\text{F1}} \sim 4 \times 10^{-7} M_{\odot} \text{ yr}^{-1}$. The radius adopted for the F1-wind is that of the bright, jet/finger-like features in the F606W *HST* images that may be footprints of the F1-wind. The agreement between our two estimates of \dot{M}_{F1} suggests that the order of magnitude obtained may be correct.

In general, very little is known about mass-loss rates of post-AGB winds, their continuous or episodic nature, and about the structure of the resulting flows after the AGB-to-'post-AGB' wind interaction. Our data indicate that the various post-AGB mass-loss episodes experienced by M 2-56 did not happen at regular time intervals, in particular, the time span between two consecutive post-AGB ejections has shortened with time. Also, according to the different expansion velocities of the distinct nebular components of M 2-56, including the molecular envelope, the successive post-AGB winds seem to be characterized by ejection speeds exponentially increasing with time. It is also worth mentioning that, unlike most pPNs and PNs with multiple optical lobes, the OLs and the ILs of M 2-56 are oriented almost identically (with their main symmetry axis inclined with respect to the line-of-sight by $i=18^\circ$; § 4.1). Since the molecular envelope has also a similar orientation, we conclude that the different post-AGB bipolar ejections in this object (except maybe for the F1-wind) have taken place along the same (or nearly the same) direction/axis over the last ~ 1400 yr. We note that, in contrast, signatures of significant jet directional changes are common amongst pPNs and PNs (e.g. Miranda et al. 1999; Sahai et al. 2007, and references therein). Another example of directionally stable jets is found in the PN He 2-90 (Guerrero et al. 2001).

We have obtained a rough estimate of the scalar linear momentum carried by the bipolar OLs, the ILs, and the F1-wind from the product of their masses (Table 3) by their maximum expansion velocities, which have been taken to be ~ 250 , 350 , and 500 km s^{-1} , respectively. In this calculation we assume that the nebular components are elongated structures with a velocity field that is mainly axial (§ 4.2). The values found ($P_{\text{OLs}} \sim 0.17 M_{\odot} \text{ km s}^{-1} > P_{\text{ILs}} \sim 0.05 M_{\odot} \text{ km s}^{-1} > P_{\text{F1}} \sim 2 \times 10^{-3} M_{\odot} \text{ km s}^{-1}$) are orders of magnitude smaller than the momentum carried by the molecular outflow, $P_{\text{mol}} \approx 10 M_{\odot} \text{ km s}^{-1}$ (in deriving this value, the linear momentum computed by Castro-Carrizo et al., 2002, $P_{\text{mol}} \sim 2 M_{\odot} \text{ km s}^{-1}$, has been corrected for our lower estimate of the CO-to-H₂ molecular abundance – see § 5). According to this, we must conclude that none of the post-AGB ejections probed by our optical data could

have transferred its large linear momentum to the CO outflow and, therefore, a primer more energetic post-AGB ejection is necessary to explain the dynamics of the molecular envelope. This result is in good accordance with the time decreasing trend of the linear momentum of the optical nebular components inferred by us ($P_{OLs} > P_{ILs} > P_{F1}$), which independently suggest (by extrapolation) that earlier post-AGB flows could have carried a larger linear momentum.

The presence of a compact dusty structure and a nuclear H II region unveiled by our data (§ 5.1 and 4.4) show evidence of further post-AGB mass-loss after the F1-wind in M 2-56. The decrease of the optical depth along the line-of-sight and along the nebular symmetry axis observed (§ 5.2) is consistent with a detached/shell-like (cocoon?) structure moving away from the central star. Assuming that the cocoon expands at constant velocity, v_c , and that the density varies with the radial distance to the star as $\rho \propto r^{-2}$ (i.e. the mass-loss rate is constant), it can be easily demonstrated that for a thick and a thin shell-like geometry:

$$v_c = r_{98} \times \left(\sqrt{\frac{N_{98}}{N_{09}}} - 1 \right) / \Delta t \quad (\text{thick shell}) \quad (6)$$

$$v_c = r_{98} \times \left(\frac{N_{98}}{N_{09}} - 1 \right) / \Delta t \quad (\text{thin shell}), \quad (7)$$

where r_{98} is the inner and mean radius of the thick and thin cocoon, respectively, in 1998, N_{98} (N_{09}) is the column density in 1998 (2009), and Δt is the time scale of the variation of the optical depth. In 1998 and 2009, the total extinction towards the star was $A_V^* = 12$ mag and 8.8 mag, respectively (§ 5.2). Subtracting the component of the extinction produced by the CO envelope and the ISM at the center, ~ 3 mag, we estimate that the V-band extinction produced by the cocoon was $A_V^{\text{cocoon}} = 12 - 3 = 9$ mag in 1998 and $A_V^{\text{cocoon}} = 8.8 - 3 = 5.8$ mag in 2009. Since the extinction is proportional to the column density, we find $N_{98}/N_{09} = 9/5.8 = 1.55$. Adopting $r_{98} \sim 0''.1$ ($\sim 3.14 \times 10^{15}$ cm, § 5.1) and $\Delta t \sim 10$ yr, the variation of the optical depth observed can be explained for moderate expansion velocities of the cocoon of $v_c \sim 30$ and 60 km s $^{-1}$ for the thin and thick shell approximation, respectively.

In the previous expanding cocoon scenario, the detached geometry (needed to explain the decrease of the optical depth) implies that the mass-loss process that led to this structure had already ended in 2009. The compact size of the cocoon, which is well inside the ILs and plausibly closer to the star than the F1-wind, suggest it is at least as young as the latter (i.e., $t_{\text{kin}} < 10$ yr). Adopting an expansion velocity of $v_c = 500$ km s $^{-1}$ as for the F1-wind, which is not unreasonable given the increasing trend of the expansion velocity of the multiple post-AGB winds of M 2-56, we obtain $t_{\text{kin}} \lesssim 2$ yr.

The presence of compact cocoons enshrouding the central source has been suggested in several pPNs. For example, the so-called *searchlight beam* features that are observed emerging from the nebular core in an increasing number of pPNs and PNs (of which CRL 2688 remains as the best known example) have been hypothesized to result from starlight escaping through holes/cavities in an inner dust cocoon (Sahai et al. 1998; Sánchez Contreras et al. 2007). Since these cocoons have not been *directly* detected, their existence remains speculative so far. We cannot rule out that the large obscuration of the central source of M 2-56 both along the lobes and the equatorial plane could also be produced by *two* distinct nebular components, namely, a dusty bipolar flow and an equatorial disk/torus, rather than by a unique cocoon-like structure. Direct observations of the obscured, innermost regions of M 2-56 using, for example, high-angular resolution techniques in the infrared and mm-wavelength range are crucial to characterize the circumstellar geometry at the nebula’s heart.

Finally, our spectra taken in 2009 have revealed a compact H II region around the central star of M 2-56 that may represent the very latest (current?) mass-loss episode of this object. It is possible that such a compact H II region was already formed in 1998 but its light, like the stellar radiation, was heavily blocked from our view by the dusty cocoon. Only due to the recent decrease of the optical depth of the latter, the emission from the H II region has been able to reach the lobes where it is scattered by the nebular dust, enabling its indirect detection. Alternatively, it is also possible that the H II region has formed recently (after 2000). In the following, we discuss this possibility in some detail. The recent formation of the H II region would imply an equally recent and rapid evolution (in less than ~ 10 yr) of the central star towards higher effective temperatures, needed to explain the raise of photonionizing UV radiation and detectable H α emission from the ionized regions. Although a large increase of T_{eff} is not deduced from our multi-epoch spectroscopic data, which do not show significant changes in the stellar spectrum⁶, a low/moderate increase of the stellar temperature from a B 0.5 to a B 0 spectral type ($\Delta T_{\text{eff}} \sim 3000$ K) is simultaneously consistent with a stable B-type classification and with a large increase of the H α equivalent width from $W_{\lambda} = 50$ to 300 \AA (for details, see Sánchez Contreras et al. 2008). The T_{eff} evolutionary rate value deduced in this case, $\Delta T_{\text{eff}} / \Delta t \gtrsim 3000 / 10 \sim 300 \text{ K yr}^{-1}$, is larger than that expected for the central star of M 2-56 based on theoretical evolutionary models for post-AGB objects taking into account the low luminosity and, thus, initial mass of this object (e.g. Bloeker 1995; van Hoof et al. 1997). However, these models assume constant values for the post-AGB mass-loss rate of 10^{-7} - $10^{-8} M_{\odot} \text{ yr}^{-1}$, single-star evolution scenarios, and other simplifying hypothesis that may not be appropriate for M 2-56. In particular, we do not rule out that the latest sudden mass ejections leading to the F1-wind and the compact cocoon, could have

⁶except for its brightening as a result of the decrease of the cocoon optical depth – see § 5.

sped up/boost the evolution of the central star towards slightly higher T_{eff} and the recent emergence of a nuclear H II region in just a few years.

In addition to the central H II region, there are probably shocks currently happening at the innermost circumstellar regions of this fascinating object as evidenced by the recent emergence of Fe II lines from the nucleus (§ 3.2.2). These Fe II lines are known to be good tracers of astrophysical shocks, e.g., in supernovae, Herbig Haro objects, PNe, etc (e.g. Welch et al. 1999; Reipurth et al. 2000). The presence of shocks at the nebula’s core suggests current, fast stellar ejections (in agreement with the broad nuclear H α profile) interacting hydrodynamically with the material in the close environment of the star ejected in earlier mass-loss episodes with smaller velocities. High-angular resolution optical imaging and spectroscopy are needed to properly study the spatio-kinematic structure of the innermost nebular regions and to attempt understanding the complex mass-loss history of the latest post-AGB ejections in M 2-56.

8. Summary

We report multi-epoch long-slit spectra at various slit positions and direct images in the optical of the pPN M 2-56. These data have allowed us to describe the spatio-kinematic structure and complex (currently active?) mass-loss history of this object with unprecedented detail.

- Our data probe several nebular components, namely, two pairs of nested, co-axial lobes with different sizes and a large contrast in surface brightness referred to as the faint outer lobes (OLs) and the bright inner lobes (ILs), a compact bipolar flow (the F1-wind), and an equatorially expanding central structure. A compact circumstellar structure obscuring the star (cocoon?) and a nuclear H II region, both spatially unresolved, are also inferred from our data.
- The optical lobes are oriented along the East-West direction (PA=90°) and their symmetry axis is inclined $\sim 18^\circ$ (with respect to the plane of the sky), similarly to the hourglass-shaped molecular envelope that surrounds the optical nebula (Castro-Carrizo et al. 2002).
- The OLs and the ILs have an overall axial symmetry and are characterized by an expansive kinematics with the velocity increasing with the distance to the nebula center, except for the outermost OLs-caps, which show reduced speeds relative to their innermost regions. The maximum velocity reached by the OLs (ILs) is $\sim 250 \text{ km s}^{-1}$

($\sim 350 \text{ km s}^{-1}$). Consistent with the large speeds observed at the tips of the ILs, we measure proper motions ($\Delta\theta_t \sim 0''.03 \text{ yr}^{-1}$) by comparing two-epoch *HST* images.

- In 1998, we detected a burst of $\text{H}\alpha$ emission from the nebula nucleus (referred to as “feature F1”) that has vanished in less than 2.9 yr. We believe that feature F1 arises in a dense, fast ($\sim 350\text{-}500 \text{ km s}^{-1}$) bipolar wind ejected after 1989 as a short-time mass-loss event.
- The mass in the OLs, ILs, and F1-wind is $M_{\text{OLs}} \sim 7 \times 10^{-4} M_{\odot}$, $M_{\text{ILs}} \sim 1.2 \times 10^{-4} M_{\odot}$, and $M_{\text{F1}} \lesssim 4 \times 10^{-6} M_{\odot}$, respectively.
- The p-v distribution of the [S II]6716/6731 line ratio has led to the discovery of a dense ($n_e \gtrsim 10^4 \text{ cm}^{-3}$), equatorial flow. The radial velocity increases approximately linearly with the distance to the center, reaching values of up to $\sim 100 \text{ km s}^{-1}$. It is possible that the equatorial flow and the OLs both resulted from a single, sudden mass-loss event that took place simultaneously along the axis and in the perpendicular plane.
- We infer the presence of a compact ($< 200 \text{ AU}$), dusty structure (cocoon?) enshrouding the central star. The optical depth of this structure has decreased a few magnitudes both along the line-of-sight and along the optical lobes in $\lesssim 10 \text{ yr}$. This has enabled a fraction of the light from the nebula’s core to escape the stellar vicinity and reach the lobes where it is scattered off by nebular dust, leading to a brightening of the scattered stellar continuum and the increase of scattered $\text{H}\alpha$ emission along the lobes in 2009.
- The scattered $\text{H}\alpha$ emission detected in 2009 along the lobes arises most likely from a compact H II region around the star.
- In 2009, we have discovered a number of permitted emission lines arising from the nucleus. The detection of Fe II lines suggests the presence of shocks at the stellar neighborhood resulting from current stellar wind activity.
- The kinematical ages of the main nebular components of M 2-56 are different from each other: $t_k \sim 1400 \text{ yr}$ for the molecular bipolar flow, $t_k \sim 300\text{-}400 \text{ yr}$ for the OLs and the equatorial flow, $t_k \sim 40 \text{ yr}$ for the ILs, $t_k \lesssim 10 \text{ yr}$ for the F1-wind, and even smaller for the compact cocoon and H II region.
- The rapid evolution of M 2-56 is driven by multiple episodes of mass ejection, that is, through a gusty or episodic post-AGB wind, that has led to the nested bipolar morphology of the nebula and the younger nuclear components discovered in this work. The duration of each of such ejections may be a small fraction of its kinematical age, which implies extremely short life-times, of a few years or less, for some of the mass-loss episodes in M 2-56.

- The various post-AGB mass ejection events experienced by M 2-56 did not happen at regular time intervals, in particular, the time span between two consecutive post-AGB ejections has shortened with time.
- The successive multiple post-AGB winds in M 2-56 are characterized by ejection speeds increasing with time from 200 to $\gtrsim 500 \text{ km s}^{-1}$. In contrast, the mass-loss rate and linear momentum may show a time decreasing trend. None of the post-AGB ejections probed by our optical data could have transferred its large linear momentum to the molecular outflow ($P_{\text{mol}} \approx 10 M_{\odot} \text{ km s}^{-1}$) and, therefore, a primer more energetic post-AGB ejection is necessary to explain the dynamics of the molecular envelope.

In summary, the data presented here indicate that we are witnessing the current, variable wind activity at the core of M 2-56 and the rapid evolution of the shocked nebular material in very short time scales. This makes of M 2-56 a unique object for studying the yet poorly known processes responsible for nebular post-AGB evolution through follow up studies. New hydrodynamical simulations of the AGB-to-'post-AGB' wind interaction using input parameters for the post-AGB wind in accordance with observational properties deduced from this work may be very useful for improving our understanding of PN/pPN shaping and evolution. For example, post-AGB winds in the form of a series of sudden, short-lived ejection events (not necessarily regularly spaced in time) should be considered. Also, models should allow for time variations not only in the velocity of the fast wind but also in its mass-loss rate and linear momentum.

We are grateful to the anonymous referee for his/her valuable comments. We thank Jorge García Rojas for performing the service mode observations of M 2-56 with the INT+WFC and NOT+ALFOSC. The INT is operated on the island of La Palma by the Isaac Newton Group in the Spanish Observatorio del Roque de los Muchachos of the Instituto de Astrofísica de Canarias. Part of the data presented here has been taken using ALFOSC, which is owned by the Instituto de Astrofísica de Andalucía (IAA) and operated at the Nordic Optical Telescope under agreement between IAA and the NBIfAFG of the Astronomical Observatory of Copenhagen. This work has been partially performed at Laboratorio de Astrofísica Espacial y Física Fundamental (LAEFF-CAB) and has been partially supported by the Spanish MICINN through grants AYA 2006-14876, AYA2009-07304, and CONSOLIDER INGENIO 2010 for the team “Molecular Astrophysics: The Herschel and Alma Era – ASTROMOL” (ref.: CSD2009-00038), and by DGU of the CM under IV-PRICIT project S-0505/ESP-0237 (ASTROCAM). LFM is supported partially by grant AYA2008-01934 of the Spanish MICINN (co-funded by FEDER funds), grant FGM-1747 of the Junta de Andalucía, and grants INCITE09E1R312096ES and INCITE09312191PR of the galician INCITE research

programme of the Dirección Xeral de Investigación, Desenvolvemento e Innovación of the Spanish Xunta de Galicia. This research has made use of the SIMBAD database, operated at CDS, Strasbourg, France, and NASA's Astrophysics Data System.

Facilities: INT NOT

REFERENCES

- Aaquist, O. B., & Kwok, S. 1990, *A&AS*, 84, 229
- Alcolea, J., Neri, R., & Bujarrabal, V. 2007, *A&A*, 468, L41
- Balick, B., & Frank, A. 2002, *ARA&A*, 40, 439
- Bloecker, T. 1995, *A&A*, 299, 755
- Bujarrabal, V., Castro-Carrizo, A., Alcolea, J., & Sánchez Contreras, C. 2001, *A&A*, 377, 868
- Cardelli, J. A., Clayton, G. C., & Mathis, J. S. 1989, *ApJ*, 345, 245
- Castro-Carrizo, A., Bujarrabal, V., Sánchez Contreras, C., Alcolea, J., & Neri, R. 2002, *A&A*, 386, 633
- Cohen, M., & Kuhl, L. V. 1977, *PASP*, 89, 829
- Cox, P., Lucas, R., Huggins, P. J., Forveille, T., Bachiller, R., Guilloteau, S., Maillard, J. P., & Omont, A. 2000, *A&A*, 353, L25
- Goodrich, R. W. 1991, *ApJ*, 376, 654 (G91)
- Guerrero, M. A., Miranda, L. F., Chu, Y.-H., Rodríguez, M., & Williams, R. M. 2001, *ApJ*, 563, 883
- Gurzadyan, G. A. 1997, *The Physics and Dynamics of Planetary Nebulae*, Springer-Verlag Berlin Heidelberg New York. Also *Astronomy and Astrophysics Library*.
- Hartigan, P., Raymond, J., & Hartmann, L. 1987, *ApJ*, 316, 323
- Hartigan, P., Morse, J. A., & Raymond, J. 1994, *ApJ*, 436, 125
- Imai, H., Obara, K., Diamond, P. J., Omodaka, T., & Sasao, T. 2002, *Nature*, 417, 829
- Imai, H. 2007, *IAU Symposium*, 242, 279

- van Hoof, P. A. M., Oudmaijer, R. D., & Waters, L. B. F. M. 1997, MNRAS, 289, 371
- Howarth, I. D. 1983, MNRAS, 203, 301
- Kwok, S. 2000, The origin and evolution of planetary nebulae / Sun Kwok. Cambridge ; New York : Cambridge University Press, 2000. (Cambridge astrophysics series ; 33)
- Mendoza, C. 1983, IAU Symp. 103: Planetary Nebulae, 103, 143
- Miranda, L. F., Guerrero, M. A., & Torrelles, J. M. 1999, AJ, 117, 1421
- Miranda, L. F., Ayala, S., Vázquez, R., & Guillén, P. F. 2006, A&A, 456, 591
- Osterbrock, D. E., & Ferland, G. J. 2006, Astrophysics of gaseous nebulae and active galactic nuclei, 2nd. ed. by D.E. Osterbrock and G.J. Ferland. Sausalito, CA: University Science Books, 2006,
- Raymond, J. C. 1979, ApJS, 39, 1
- Reipurth, B., Yu, K., Heathcote, S., Bally, J., & Rodríguez, L. F. 2000, AJ, 120, 1449.
- Riera, A., Binette, L., & Raga, A. C. 2006, A&A, 455, 203
- Sahai, R., & Trauger, J. T. 1998, AJ, 116, 1357
- Sahai, R., et al. 1998, ApJ, 493, 301
- Sahai, R., Morris, M., Sánchez Contreras, C., & Claussen, M. 2007, AJ, 134, 2200
- Sánchez Contreras, C., Sahai, R., Gil de Paz, A., & Goodrich, R. 2008, ApJS, 179, 166
- Sánchez Contreras, C., Le Mignant, D., Sahai, R., Gil de Paz, A., & Morris, M. 2007, ApJ, 656, 1150
- Sánchez Contreras, C., Sahai, R., & Gil de Paz, A. 2002, ApJ, 578, 269
- Sánchez Contreras, C., & Sahai, R. 2001, ApJ, 553, L173
- Sánchez Contreras, C., Bujarrabal, V., Miranda, L. F., & Fernández-Figueroa, M. J. 2000, A&A, 355, 1103
- Siódmiak, N., Meixner, M., Ueta, T., Sugerman, B. E. K., Van de Steene, G. C., & Szczerba, R. 2008, ApJ, 677, 382
- Solf, J. 2000, A&A, 354, 674

- Suárez, O., Gómez, J. F., Miranda, L. F., Torrelles, J. M., Gómez, Y., Anglada, G., & Morata, O. 2009, *A&A*, 505, 217
- Trammell, S. R., Dinerstein, H. L., & Goodrich, R. W. 1993, *ApJ*, 402, 249
- Ueta, T., Murakawa, K., & Meixner, M. 2007, *AJ*, 133, 1345
- Velázquez, P. F., Riera, A., & Raga, A. C. 2004, *A&A*, 419, 991
- Welch, C. A., Frank, A., Pipher, J. L., Forrest, W. J., & Woodward, C. E. 1999, *ApJ*, 522, L69.

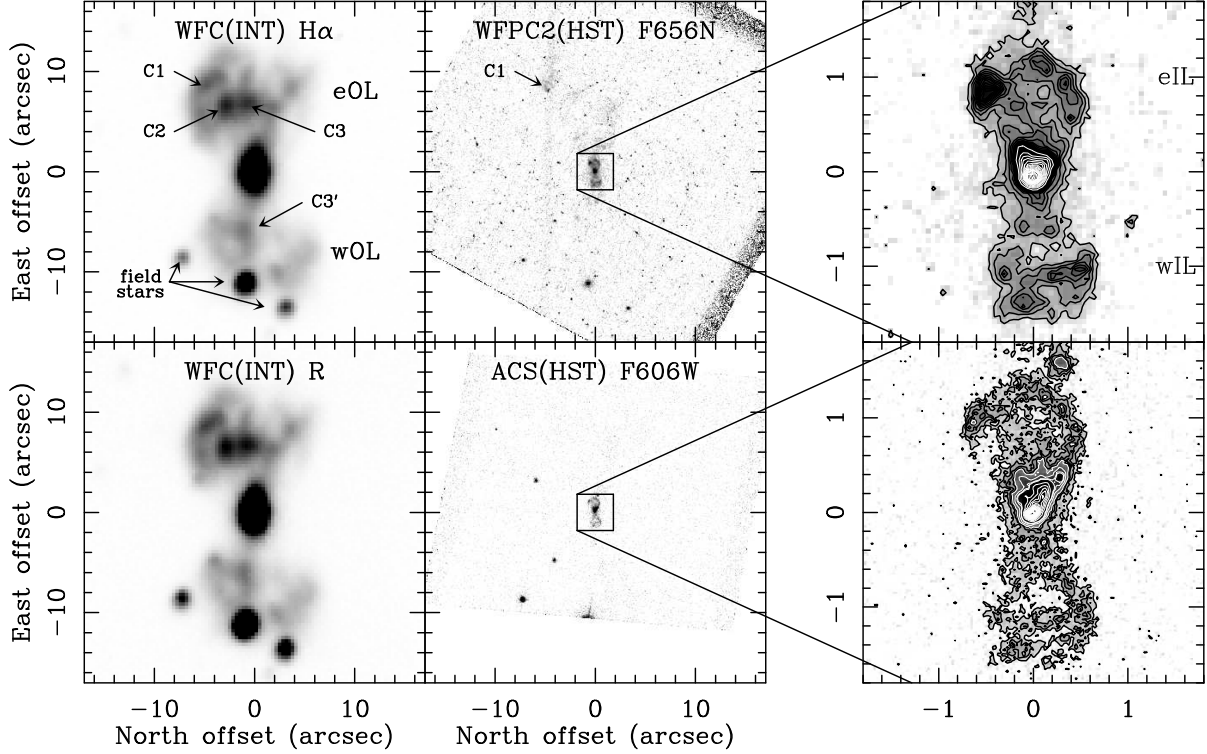


Fig. 1.— **Left)** Images of M2-56 obtained with the WFC of the 2.5 m INT through the narrow $H\alpha$ and R broad-band filters (top and bottom, respectively) plotted using a logarithmic scale. The faint, extended east and west outer lobes (eOL and wOL), nebular condensations C1, C2, C3, and C3', and field stars are labeled. **Middle)** Images obtained with the *HST* through the F656N ($H\alpha$) and F606W filters (top and bottom, respectively) plotted using a logarithmic scale. The bright, compact east and west inner lobes are labeled (eIL and wIL). **Right)** Inset of the *HST* images (FoV= $3''.6 \times 3''.6$) showing the small-scale structure of the inner nebular lobes.

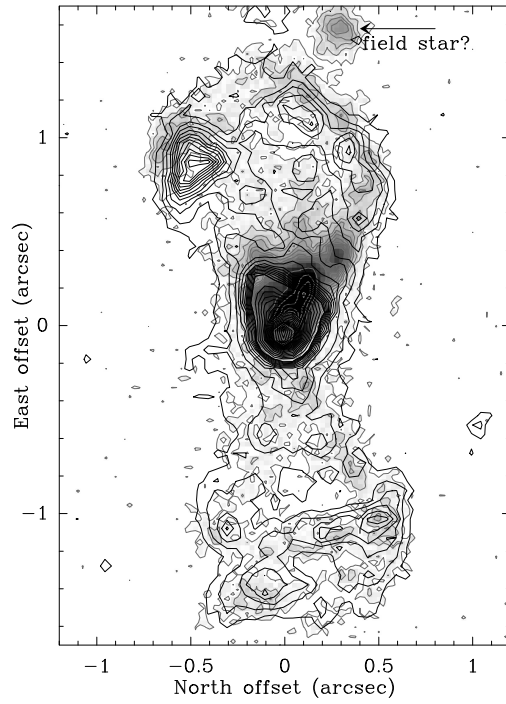


Fig. 2.— *HST* images of the ILs of M 2-56 observed in 2002 with the F606W filter (color scale and blue contours) and in 1998 with the F656N filter (green contours) showing the proper motions of the tips of the lobes and other structural differences within their innermost regions (closest to the center).

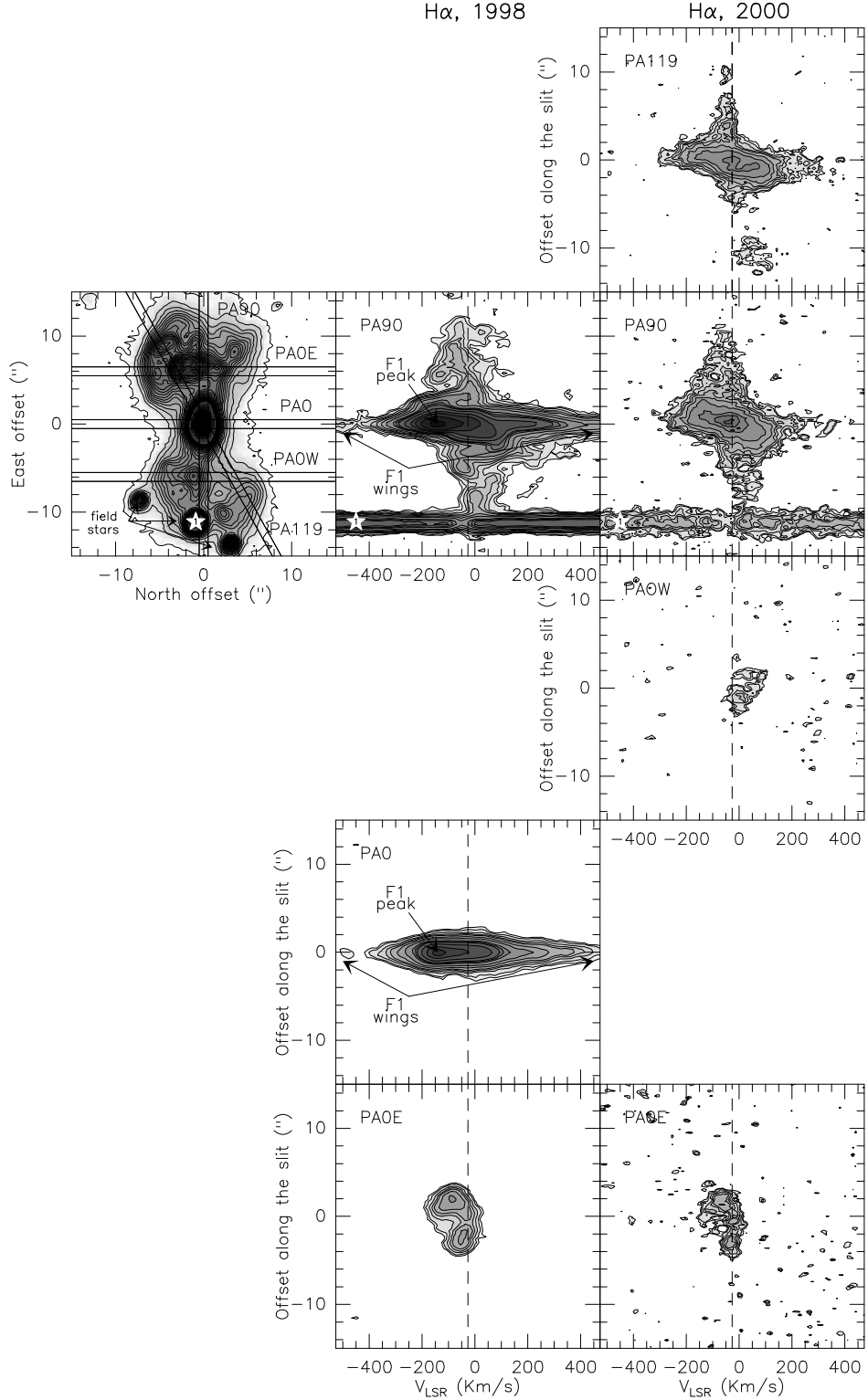
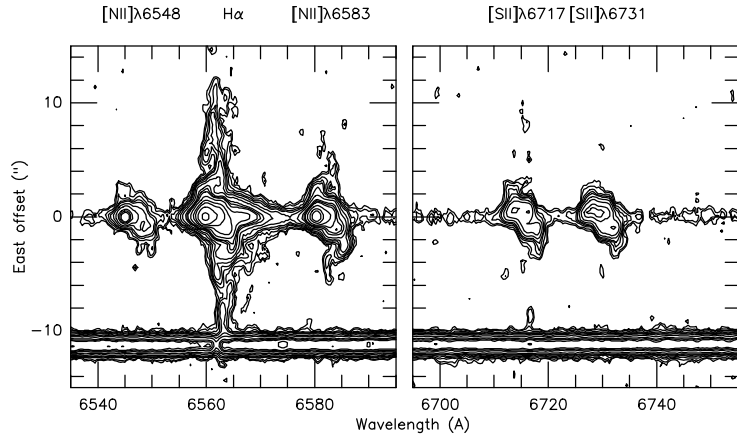


Fig. 3.— Long-slit $H\alpha$ spectra in M2-56 for the five slit positions observed in our 1998 and 2000 runs. The ground-based $H\alpha$ image of the nebula is shown on the leftmost panel; slit positions are superimposed on the image. The origin of the spatial scale in the spectra coincides with the point of maximum continuum and $H\alpha$ emission. The LSR systemic velocity of the source, $V_{\text{sys}} = -27 \text{ km s}^{-1}$, is indicated by a vertical dashed line on each spectrum. The intense, blue-shifted emission feature at the nebula center observed in 1998 and its broad

PA90 1998



PA90 2000

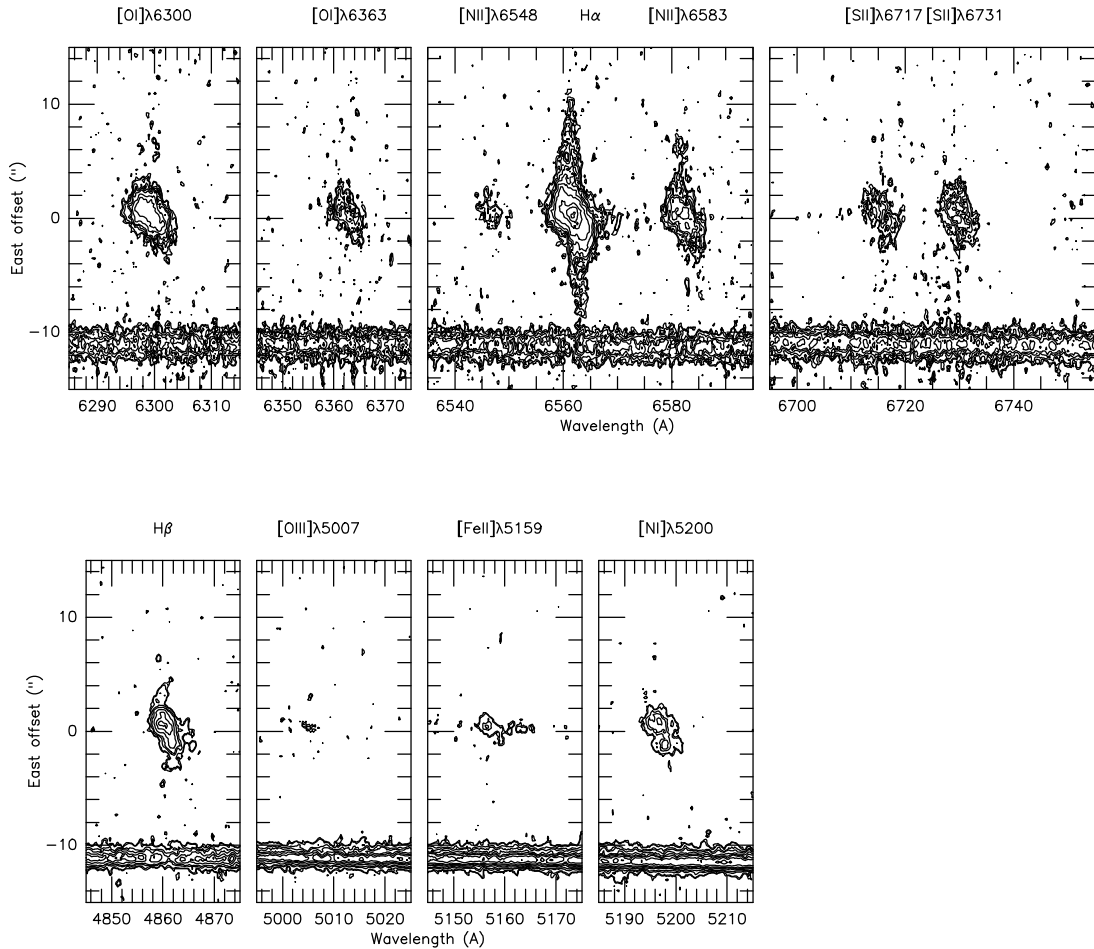


Fig. 4.— Long-slit spectra over the whole spectral range observed in 1998 and 2000 for the central slit PA90 (see Table 1 and Fig. 3).

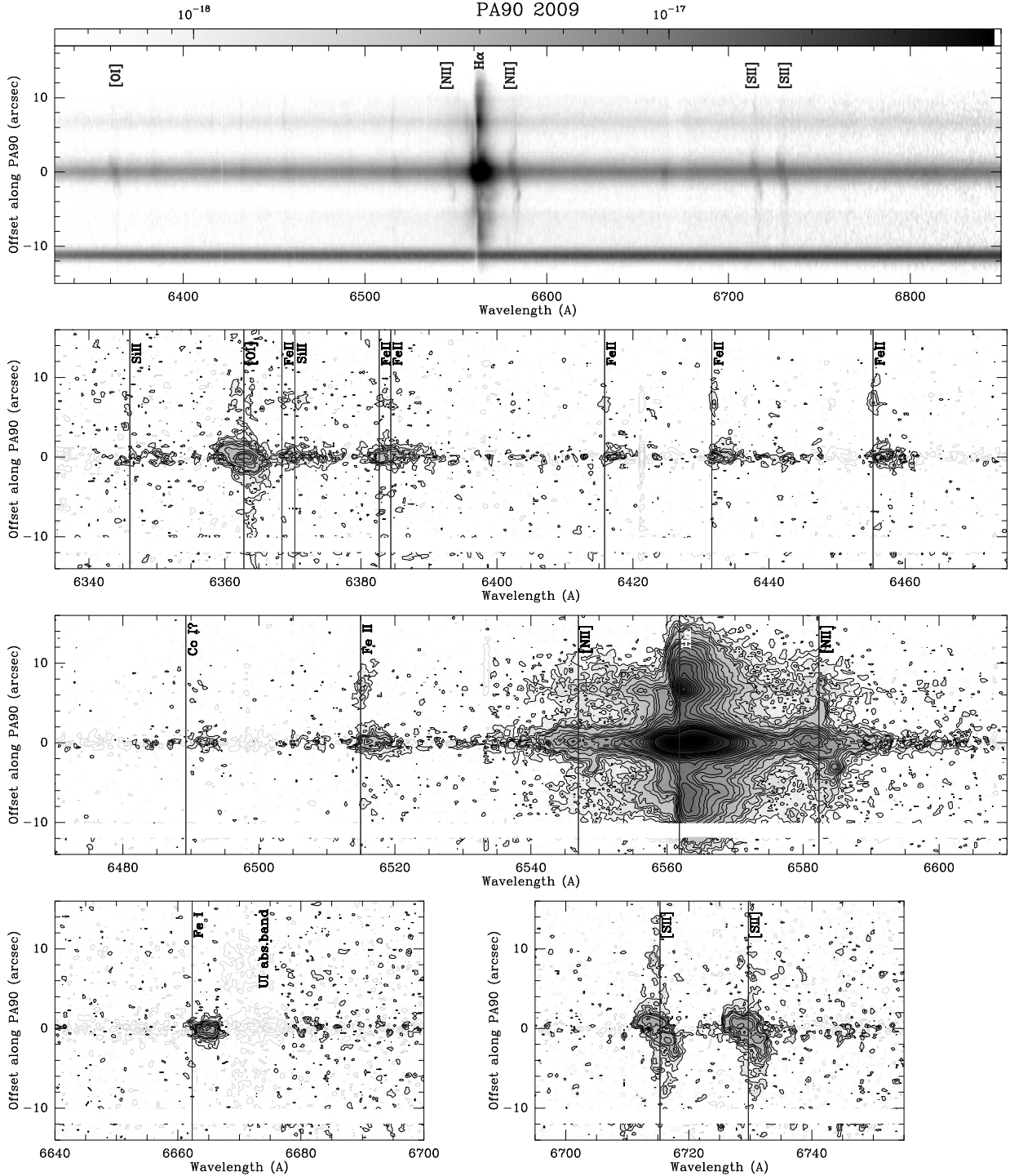


Fig. 5.— **Top panel)** Long-slit spectrum for slit PA90 obtained in 2009 in a logarithmic color scale. The spectrum has been smoothed with a flat-topped rectangular kernel of dimension 3×3 pixels. The units of the wedge at the top of the box are $\text{ergs}^{-1} \text{cm}^{-2} \text{Å}^{-1} \text{arcsec}^{-1}$. **Middle and bottom panels)** Same as above but continuum subtracted and showing selected wavelength ranges. Lines detected are labeled (see Table 2). The blue vertical lines are placed at V_{sys} for each of the observed transitions. Contour levels are: 2σ , 4σ , 6σ , 8σ , 10σ , 15σ , 20σ , 25σ , 30σ , 40σ , 50σ , 60σ , from 75σ to 300σ in steps of 25σ , from 300σ to 1000σ in steps of 100σ (black), and -3σ , -6σ , -9σ ... (magenta) with $\sigma = 1.2 \times 10^{-19}$ $\text{ergs}^{-1} \text{cm}^{-2} \text{Å}^{-1} \text{arcsec}^{-1}$. All the labels are for the lines (containing the [SII] label).

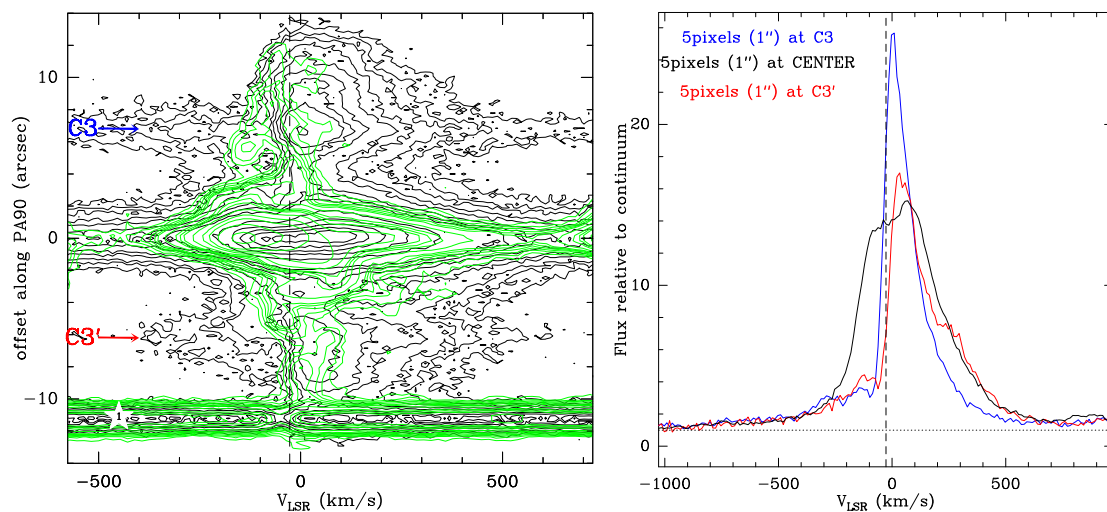


Fig. 6.— **Left)** Superposition of the H α long-slit spectrum along PA90 obtained in 2009 (grey color scale) and in 1998 (green contours). The systemic velocity is indicated by the vertical dashed line. The loci of clumps C3 and C3' along the slit is shown. **Right)** One dimensional H α profile extracted within a $1'' \times 1''$ region centered at condensations C3 (blue) and C3' (red) and at the nebula center (black).

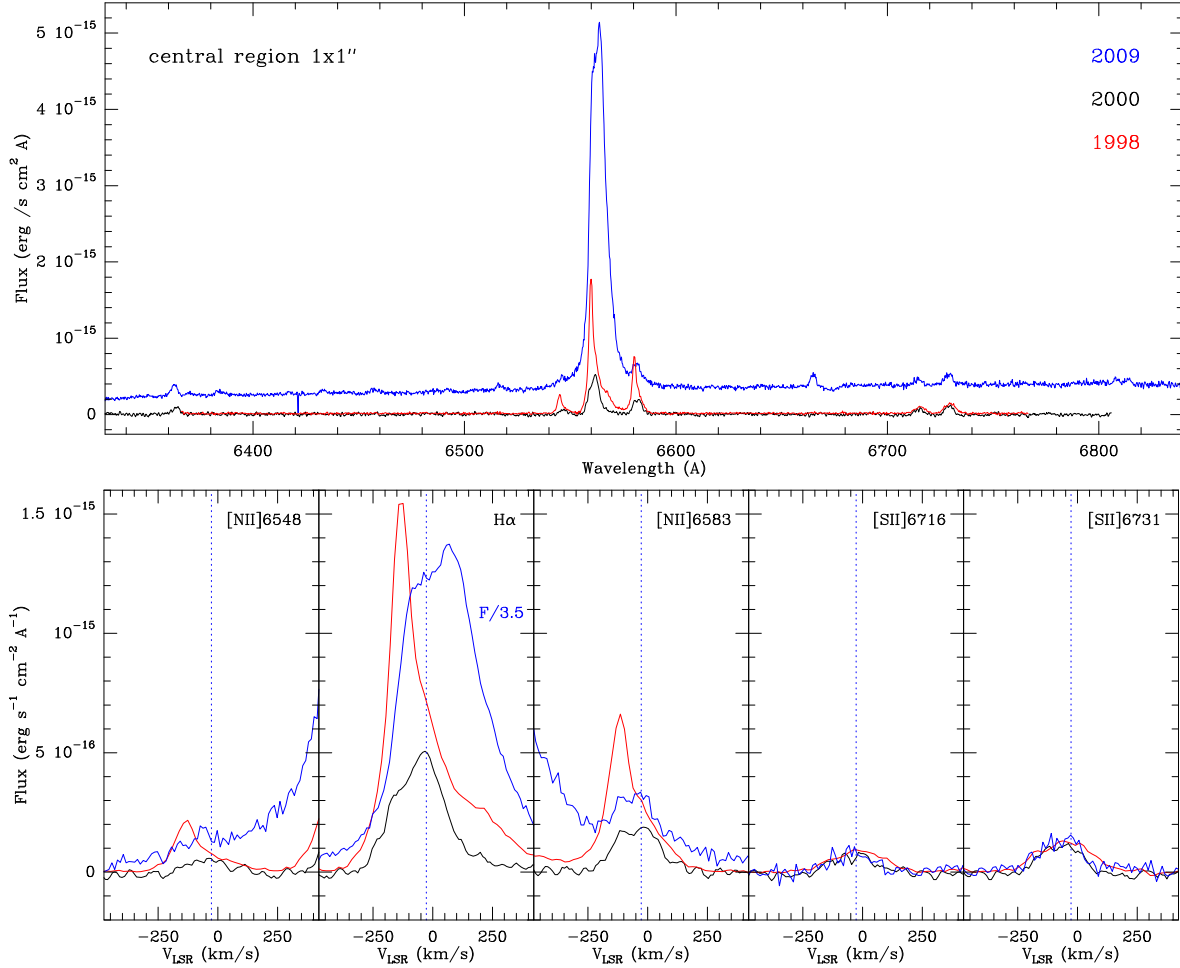


Fig. 7.— **Top)** Onedimensional spectra from a central region of $1'' \times 1''$ extracted from our long-slit spectra PA90 obtained in 1998 (black), 2000 (red), and 2009 (blue). The 1998 and 2000 spectra have been boxcar smoothed to match a common value of the dispersion of $\sim 0.7\text{\AA}$. **Bottom)** The same as in top panel after fitting and subtracting the continuum and for selected transitions detected in all three epochs using a velocity scale in the x -axis. The H α profile in 2009 has been scaled down by a factor 3.5 for an easier comparison with the weaker emission profile in 1998 and 2000. The systemic velocity is indicated by the vertical blue-dotted line. Note the similar profile of the [S II] doublet lines in all epochs and the remarkable differences in the H α and [N II] lines.

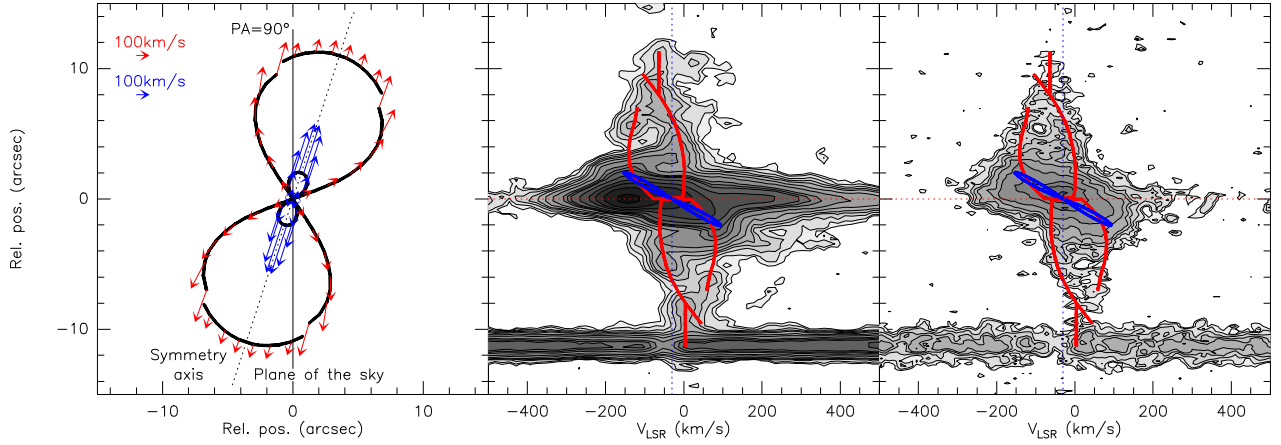


Fig. 8.— **Left)** Schematic geometry of M2-56 deduced from the model fitting (§ 4.2). This plot represents a cut of the nebula by a plane perpendicular to the plane of the sky in the direction of PA90. In this diagram $1''$ corresponds to 3.14×10^{16} cm ($d=2.1$ kpc, § 1). The velocity field in the ILs (OLs) is indicated by blue (red) arrows, respectively. **Right)** $H\alpha$ spectrum along PA90 slit orientation as observed in 1998 and 2000. The position-velocity diagrams resulting from the model fitting are superimposed. Contours and color scale are the same as in Fig. 3.

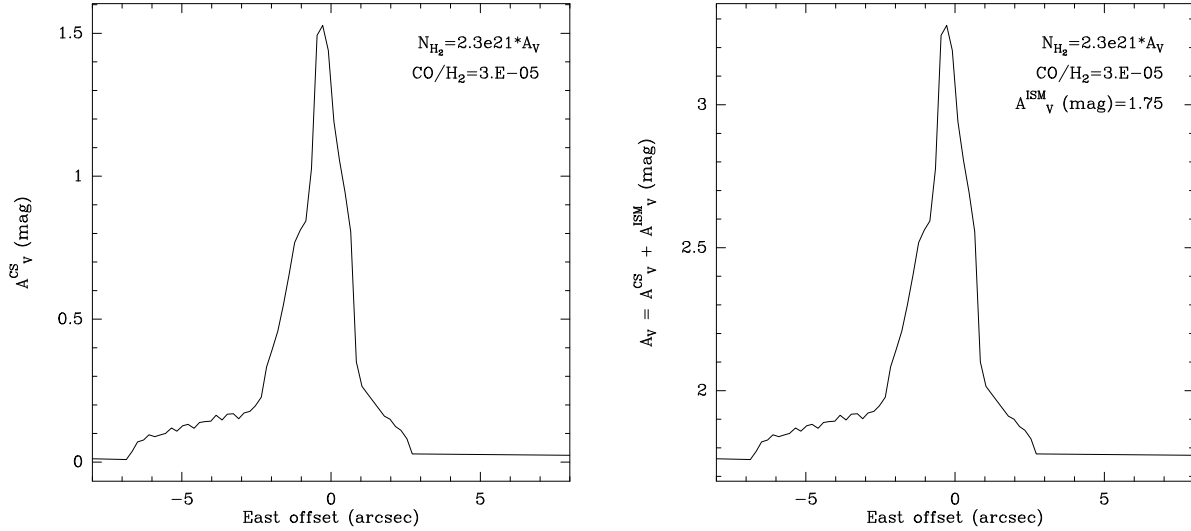


Fig. 9.— Spatial distribution of the circumstellar (left) and total, i.e. circumstellar+interstellar, extinction (right) along PA90 inferred from the model of the molecular envelope by Castro-Carrizo et al. (2002). The value for the CO-to-H₂ abundance ratio, ISM extinction, and the conversion factor between H₂ column density and dust extinction adopted are indicated.

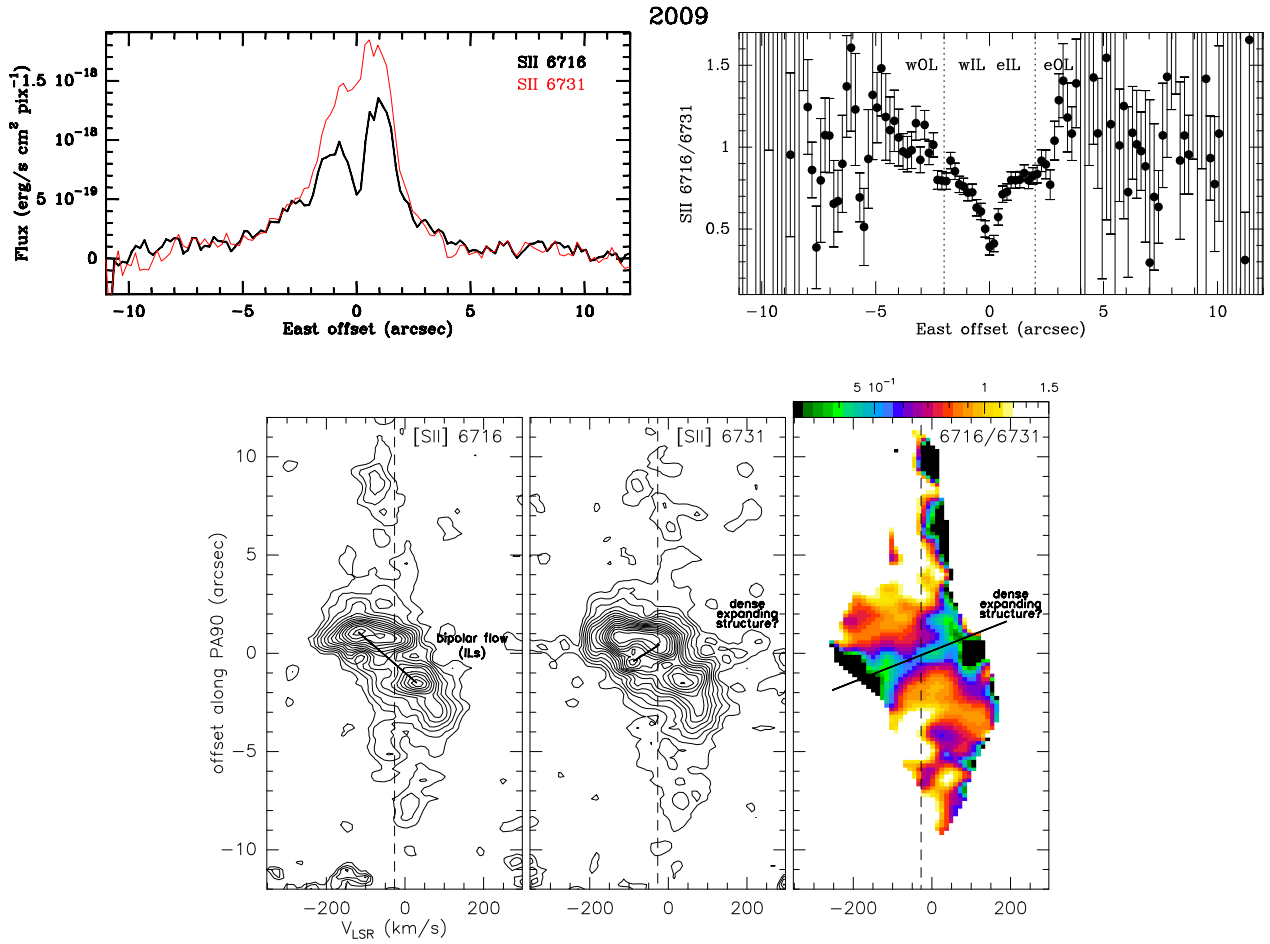


Fig. 10.— **Top**) Spatial distribution along PA90 of the lines of the [S II] $\lambda\lambda$ 6716,6732Å doublet (left) and their relative intensity (right) observed in 2009. **Bottom**) Position-velocity diagram along PA90 of the [S II] lines and their ratio observed in 2009. The p-v distribution of the 6716/6731 intensity ratio towards the center evidences a dense, equatorially expanding structure.

Table 1: Log of spectroscopic observations

Run #	Date (yyyy-mm-dd)	Telescope +Instrument	Grating	Dispersion (\AA pix^{-1})	Range (\AA)	Pixel ($''$)	Slit Position ^a	Exposure (s)
1	1998-01-17	INT+IDS	R1200Y	0.39	6370-6770	0.33	PA90	3600
1	1998-01-18	INT+IDS	R1200Y	0.39	6370-6770	0.33	PA0,PA0E	3600,3600
2	2000-11-11 ^b	INT+IDS	R1200Y	0.22	6234-6805	0.19	PA90,PA0E	10800,9000
2	2000-11-12	INT+IDS	R1200Y	0.22	6234-6805	0.19	PA0W,PA119	11700,10800
2	2000-11-13	INT+IDS	R900V	0.30	4558-5330	0.19	PA90	27300
3	2009-08-23	NOT+ALFOSC	VPH #17	0.26	6330-6850	0.19	PA90	6800

^aSee Fig. 3 for slit position labels.

^bNon-photometric conditions

Table 2. Multi-epoch line fluxes observed (F_λ) and dereddened (I_λ) for M 2-56

Line	F_λ (10^{-15} erg s $^{-1}$ cm $^{-2}$)			I_λ (10^{-15} erg s $^{-1}$ cm $^{-2}$)		
	1998	2000	2009	1998	2000	2009
H β λ 4861.3	...	1.20(0.04)	36(9)	...
[O III] λ 5006.8	...	0.07(0.04)	2.0(1.2)	...
[Fe II] $\lambda\lambda$ 5158.0,5158.8	...	0.20(0.04)	4.9(1.4)	...
[N I] λ 5200.3	...	0.65(0.04)	15(3)	...
[Fe II] λ 5261.6	...	0.05(0.04)	1.1(0.9)	...
[O I] λ 6300.3	...	6.4(0.4)	76(12)	...
[O I] λ 6363.8	...	2.0(0.4)	2.2(0.14)	...	23(6)	25(4)
Fe II $\lambda\lambda$ 6383.8,6385.5 †	1.12(0.07)	13(2)
Fe II λ 6416.9 †	0.21(0.07)	2.4(0.9)
Fe II λ 6432.7 †	0.42(0.07)	4.7(1.1)
Fe II λ 6456.4 †	0.77(0.07)	8.5(0.14)
Co I? λ 6490.3 †	0.21(0.07)	2.3(0.8)
Fe II λ 6516.1 †	0.91(0.07)	10(2)
[N II] λ 6548.0	2.3(0.2)	1.6(0.4)	4.9(1.1)	24(4)	17(5)	52(14)
H α λ 6562.8	23(0.4)	15.1(0.4)	161(1.1)	240(40)	160(6)	1700(300)
[N II] λ 6583.5	6.7(0.3)	4.8(0.4)	10.5(1.1)	70(11)	50(2)	110(20)
Fe I λ 6663.4 †	0.14(0.07)	1.4(0.2)
[S II] λ 6716.4	2.6(0.2)	2.4(0.4)	2.6(0.7)	25(4)	23(5)	25(14)
[S II] λ 6730.8	2.9(0.2)	3.2(0.4)	3.4(0.7)	28(5)	31(6)	33(14)

† Lines discovered in this work.

Note. — Errors are given in parenthesis.

Table 3: Atomic and ionized mass of M 2-56

Component	$F_{H\alpha}$ ($10^{-15} \text{ erg s}^{-1} \text{ cm}^{-2}$)	$F_{[\text{O} \text{I}]}$ ($10^{-15} \text{ erg s}^{-1} \text{ cm}^{-2}$)	$\langle A_V \rangle$ (mag)	$\langle n_e \rangle$ (cm^{-3})	$M_{H^+}^{H\alpha}$ (M_\odot)	$M_H^{[\text{O} \text{I}]}$ (M_\odot)
OLs	5.7(± 0.2)	2.0(± 0.6)	2	200	5.3×10^{-4}	1.5×10^{-4}
ILs	9.3(± 0.2)	5.4(± 0.4)	3	1500	8.2×10^{-5}	3.8×10^{-5}
F1-wind	8.0(± 0.2)	–	$\gtrsim 3$ (± 12)	$> 2.6 \times 10^4$	$4.1 \times 10^{-6\dagger}$ ($< 4.2 \times 10^{-3}$)	–

[†]Particularly uncertain. See text in § 6.2